The Journal of Chemical Physics

RESEARCH ARTICLE | SEPTEMBER 23 2025

Quantum dynamics at conical intersections in solution. I. Multiplicative neural networks and thermofields

Bartosz Błasiak ; Dominik Brey ; Rocco Martinazzo ; Irene Burghardt

J. Chem. Phys. 163, 124108 (2025)
https://doi.org/10.1063/5.0284503

The Journal of Chemical Physics ARTICLE pubs.aip.org/aip/jcp

Quantum dynamics at conical intersections in solution. I. Multiplicative neural networks and thermofields

Cite as: J. Chem. Phys. 163, 124108 (2025); doi: 10.1063/5.0284503
Submitted: 8 June 2025 • Accepted: 25 August 2025 •
Published Online: 23 September 2025

Bartosz Błasiak,[1] Dominik Brey,[1] Rocco Martinazzo,[2] and Irene Burghardt[1,a)]

AFFILIATIONS

[1] Institute of Physical and Theoretical Chemistry, Goethe University Frankfurt, Max-von-Laue-Str. 7, 60438 Frankfurt, Germany
[2] Department of Chemistry, Università degli Studi di Milano, Via Golgi 19, 20133 Milano, Italy

[a)] **Author to whom correspondence should be addressed:** burghardt@chemie.uni-frankfurt.de

ABSTRACT

Environmental effects on the vibronic dynamics at a conical intersection can be captured by collective modes, which affect both the topology of the nonadiabatically coupled potential surfaces and the transient dynamics. Here, we show how neural network (NN) potentials can be adapted to a combination of intramolecular coordinates and collective environmental modes. Specifically, we use multiplicative NN (m-NN) potentials, which are fitted to a diabatic representation of regularized diabatic states type. These potentials are readily combined with multi-configurational wave functions for high-dimensional quantum dynamics. The thermofield dynamics (TFD) approach is employed to include thermal averaging at the wave function level, and we formulate a thermal NN/TFD Hamiltonian that accommodates initial vibronic correlations and collective/residual-mode coupling in the environmental subspace. For a model system describing the isomerization of protonated Schiff bases in solution, the solvent is represented by an overdamped Brownian-oscillator spectral density. In a companion paper [B. Błasiak *et al.*, J. Chem. Phys. **163**, 124109 (2025)], the resulting m-NN/TFD Hamiltonian is employed in real-time quantum dynamical simulations using the multi-layer multiconfiguration time-dependent Hartree method.

I. INTRODUCTION

Machine learning (ML) approaches for electronically excited states and photochemical processes have made significant progress over recent years,[1–4] even though they remain challenging as compared with their ground-state counterparts. This applies, in particular, to conical intersection (CI) topologies, which play a key role in the photodynamics of polyatomic molecules. While potential fitting via neural networks[5–8] (NNs) or kernel regression methods like Gaussian process regression[9–11] generally relies on adiabatic input information, a diabatic representation[12] is often introduced for ML-based nonadiabatically coupled potential energy surfaces (PES) such as to eliminate nonadiabatic derivative couplings.[5,8,13–15] This is of particular importance if the resulting NN potentials are combined with quantum dynamical wavepacket propagation.

Against this background, we recently developed an approach[16] that adapts multiplicative neural network (m-NN) fitting[6,7] to the construction of regularized diabatic states (RDS),[17,18] which provide a flexible representation of conical intersection topologies. RDS potentials combine a linearized representation at the conical intersection with an accurate asymptotic representation of the PES.

In the present work, we show that this approach is especially suited to include environmental effects at a conical intersection. Environmental effects, e.g., due to a solvent, can significantly modify the system's topology. In particular, conical intersections can be energetically shifted, their character can be changed, e.g., from peaked to sloped,[19,20] and they can disappear altogether. Including these effects often does not require a full atomistic description, typically relying on quantum mechanics/molecular mechanics (QM/MM) schemes,[20–23] but can be achieved by treating collective effects, for example, due to the reorganization of the solvent polarization as described by Marcus theory.[24,25]

The purpose of the present work is, therefore, to show how neural network potentials for conical intersections can be extended to encompass collective variables that represent the vibronic

effects exerted by the environment. Specifically, the RDS approach permits including these collective variables on an equal footing with intramolecular chromophore modes, beyond the standard linear vibronic coupling (LVC) model.[12] Building upon earlier work on the construction of collective vibronic modes within the LVC model,[26–29] we show that an embedding of this construction into the RDS diabatization, followed by NN fitting, provides a very flexible definition of vibronic coupling potentials, including environmental modes. Within a hierarchical representation, the high-dimensional nature of the environment space is represented by a residual subspace that couples, in turn, to the collective variables.[26–29]

The dynamical effects associated with these collective environmental modes can relate, e.g., to solvent reorientational or translational motion. Indeed, the present description connects to Brownian oscillator models,[30,31] or polarization coordinate models, which have been previously used to describe nonequilibrium solvation effects.[24,25] One should note that the inclusion of specific microsolvation effects, e.g., due to hydrogen bonding, necessitates a different description, such that the molecular subsystem, i.e., the chromophore, would be augmented by the relevant degrees of freedom.

In order to account for a thermal distribution of the environment, e.g., the solvent, we employ the thermofield dynamics (TFD) approach, which represents the wave function in a duplicated Hilbert space.[32–34] The resulting effective thermal Hamiltonian determines the time evolution of the chromophore in contact with the thermal environment state. Here, we adapt the TFD approach such as to accommodate (i) initial state-specific equilibration and (ii) the hierarchical representation of the environment in terms of collective vs residual subspaces. This approach is highly convenient when combined with tensor network methods of multi-layer multiconfiguration Hartree (ML-MCTDH)[35,36] or matrix product state (MPS) type,[37,38] as illustrated in recent applications.[34,39,40] In a companion paper, henceforth referred to as Paper II,[41] we illustrate ML-MCTDH dynamics under the effect of the NN/TFD Hamiltonian developed here.

In the present study, the NN/TFD approach is applied to a model of the isomerization dynamics in protonated Schiff bases (PSB), i.e., retinal type systems, whose photochemistry is highly sensitive to solvent effects.[20,22,42–46] Similarly to Ref. 16, the NN construction is carried out, for the purpose of demonstration, for a randomly sampled dataset generated from adiabatic potentials associated with an analytically defined reference potential.[47] These potentials carry realistic features of PSB isomerization,[47,48] and they show significant deviations from an LVC model. These potentials were set up on a valence bond type basis, describing charge translocation upon photoexcitation of a PSB.[47,48] In Refs. 49 and 55, preliminary quantum dynamical simulations were reported, and in Refs. 50 and 51, this model was applied in conjunction with surface hopping simulations. In the more recent NN-based study of Ref. 16, this PSB model was again employed, but the aspect of environmental effects was not considered, which is central to the present work. Furthermore, in the present model, the NN potentials have been significantly improved by adaptation to the periodic nature of the potential.

The remainder of the paper is structured as follows. Section II shows how the collective/residual mode representation of the environment is integrated into more flexible regularized diabatic state potentials. Section III describes the neural network approach, and Sec. IV focuses on the thermofield description. Section V concludes with a discussion.

II. VIBRONIC COUPLING INCLUDING ENVIRONMENTAL EFFECTS

Environment-induced vibronic coupling effects have been extensively investigated in the context of the spin-boson Hamiltonian and many applications to charge transfer and energy transfer. In the following, the discussion is adapted to the more complex topology of conical intersections, following Refs. 26–29 and 52.

A. Collective modes at a conical intersection

Environmental effects at a conical intersection are typically multi-mode effects that are not constrained by the symmetry elements of the molecular subsystem. In the case of symmetry-allowed conical intersections, environmental fluctuations can therefore act both in a symmetry-conserving or symmetry-breaking way. However, despite the multi-mode character of the dynamics, the dominant vibronic effects of the environment can be shown to be mediated by few collective variables, or effective modes.[26–29,52]

Our starting point is a general diabatic vibronic coupling Hamiltonian for the system modes $\{\widehat{q}_{S,i}\}$ and bath modes $\{\widehat{q}_{B,i}\}$,

$$\begin{aligned}\widehat{\boldsymbol{H}}(\widehat{\boldsymbol{q}}_S,\widehat{\boldsymbol{q}}_B) &= \widehat{H}^0_S(\widehat{\boldsymbol{q}}_S) + \widehat{H}^0_B(\widehat{\boldsymbol{q}}_B) + \widehat{\boldsymbol{V}}_{\rm VC}(\widehat{\boldsymbol{q}}_S,\widehat{\boldsymbol{q}}_B)\\ &= \sum_{i=1}^{N_S}\frac{\omega_{S,i}}{2}(\widehat{p}^2_{S,i}+\widehat{q}^2_{S,i})\mathbf{1} + \sum_{i=1}^{N_B}\frac{\omega_{B,i}}{2}(\widehat{p}^2_{B,i}+\widehat{q}^2_{B,i})\mathbf{1}\\ &\quad + \widehat{\boldsymbol{V}}_{\rm VC}(\widehat{\boldsymbol{q}}_S,\widehat{\boldsymbol{q}}_B),\end{aligned} \tag{1}$$

where mass and frequency weighted coordinates are employed, the momentum operators are given as $\widehat{p}_i = -i\partial/\partial q_i$, and the kinetic energy is electronically diagonal. The vibronic coupling (VC) potential $\widehat{\boldsymbol{V}}_{\rm VC}$ contains both diagonal and off-diagonal vibronic coupling terms. Due to the high dimensionality of the environmental space, the linear vibronic coupling approximation is a good starting point. If the LVC approximation is made for the bath subspace but not for the system subspace, the following quasi-diabatic Hamiltonian results for a two-state system:

$$\widehat{\boldsymbol{V}}_{\rm VC}(\widehat{\boldsymbol{q}}_S,\widehat{\boldsymbol{q}}_B) = \begin{pmatrix} \widehat{v}_{11}(\widehat{\boldsymbol{q}}_S) + \sum_i \kappa^{(1)}_{B,i}\widehat{q}_{B,i} & \widehat{v}_{12}(\widehat{\boldsymbol{q}}_S) + \sum_i \lambda_{B,i}\widehat{q}_{B,i} \\ \widehat{v}_{12}(\widehat{\boldsymbol{q}}_S) + \sum_i \lambda_{B,i}\widehat{q}_{B,i} & \widehat{v}_{22}(\widehat{\boldsymbol{q}}_S) + \sum_i \kappa^{(2)}_{B,i}\widehat{q}_{B,i}\end{pmatrix}. \tag{2}$$

In general, each individual environmental (bath) mode can couple both diagonally and off-diagonally to the electronic subsystem. If the LVC representation is employed for the subsystem, too, we further approximate $\widehat{v}_{nn} = \sum_i \kappa^{(n)}_{S,i}\widehat{q}^{\,t}_{S,i}$ and $\widehat{v}_{nn'} = \sum_i \lambda^{(n)}_{S,i}\widehat{q}^{\,c}_{S,i}$, $n \neq n'$, where the superscripts t and c denote tuning modes and coupling modes, respectively.[12,53]

Following Refs. 26–29 and 52, we now make use of the fact that the environmental modes produce cumulative effects in the vibronic coupling to the electronic subsystem. The vibronic contributions by

the $\{\widehat{q}_{B,i}\}$ modes according to Eq. (2) can, therefore, be absorbed into a set of collective coordinates $(\widehat{Q}_{B,+}, \widehat{Q}_{B,-}, \widehat{Q}_{B,\Lambda})$,

$$\widehat{\boldsymbol{V}}_{\mathrm{VC}}(\widehat{\boldsymbol{q}}_S, \widehat{\boldsymbol{Q}}_B) = \begin{pmatrix} \widehat{v}_{11}(\widehat{\boldsymbol{q}}_S) + (\widehat{Q}_{B,+} + \widehat{Q}_{B,-}) & \widehat{v}_{12}(\widehat{\boldsymbol{q}}_S) + \widehat{Q}_{B,\Lambda} \\ \widehat{v}_{12}(\widehat{\boldsymbol{q}}_S) + \widehat{Q}_{B,\Lambda} & \widehat{v}_{22}(\widehat{\boldsymbol{q}}_S) + (\widehat{Q}_{B,+} - \widehat{Q}_{B,-}) \end{pmatrix}, \tag{3}$$

where collective, or effective modes are defined as

$$\begin{aligned} \widehat{Q}_{B,+} &= \frac{1}{2}\sum_i (\kappa_{B,i}^{(1)} + \kappa_{B,i}^{(2)})\widehat{q}_{B,i}, \\ \widehat{Q}_{B,-} &= \frac{1}{2}\sum_i (\kappa_{B,i}^{(1)} - \kappa_{B,i}^{(2)})\widehat{q}_{B,i}, \\ \widehat{Q}_{B,\Lambda} &= \sum_i \lambda_{B,i}\widehat{q}_{B,i}. \end{aligned} \tag{4}$$

These three variables reflect collective shift $(\widehat{Q}_{B,+})$, tuning $(\widehat{Q}_{B,-})$, and coupling $(\widehat{Q}_{B,\Lambda})$ effects exerted by the environment upon the electronic subsystem. Specifically, the mode $\widehat{Q}_{B,-}$ describes environment-induced energy-gap fluctuations. The coordinates $(\widehat{Q}_{B,-}, \widehat{Q}_{B,\Lambda})$ reflect the projection of the branching plane vectors[19] on the bath subspace, whereas the $\widehat{Q}_{B,+}$ coordinate lies on the conical intersection seam. For more than two electronic states, $\frac{1}{2}N(N+1)$ collective modes are obtained.[54]

Since the collective coordinates of Eq. (4) are not orthogonal (and not normalized), an additional transformation is necessary, leading to orthogonal effective modes $(\widehat{Q}_{B,1}, \widehat{Q}_{B,2}, \widehat{Q}_{B,3})$. Using a topology-adapted representation,[28] the orthogonal vectors $(\widehat{Q}_{B,2}, \widehat{Q}_{B,3})$ span the environmental subspace of the branching plane,

$$\begin{aligned} \widehat{\boldsymbol{V}}_{\mathrm{VC}}(\widehat{\boldsymbol{q}}_S, \widehat{\boldsymbol{Q}}_B) &= \sum_{i=1}^{3} K_{B,i}\widehat{Q}_{B,i} \\ &+ \begin{pmatrix} \widehat{v}_{11}(\widehat{\boldsymbol{q}}_S) + \sum_{i=2}^{3} D_{B,i}\widehat{Q}_{B,i} & \widehat{v}_{12}(\widehat{\boldsymbol{q}}_S) + \Lambda_B\widehat{Q}_{B,3} \\ \widehat{v}_{12}(\widehat{\boldsymbol{q}}_S) + \Lambda_B\widehat{Q}_{B,3} & \widehat{v}_{22}(\widehat{\boldsymbol{q}}_S) - \sum_{i=2}^{3} D_{B,i}\widehat{Q}_{B,i} \end{pmatrix}. \end{aligned} \tag{5}$$

The three effective modes $(\widehat{Q}_{B,i})$, $i = 1, \ldots, 3$, are part of an orthogonal transformation within the N_B-dimensional bath subspace, $\widehat{\boldsymbol{Q}} = \boldsymbol{T}\widehat{\boldsymbol{q}}$.[26–29] As a consequence of this transformation, the effective modes are distinguished from the residual modes $(\widehat{Q}'_{B,i})$, $i = 1, \ldots, N_{\mathrm{res}}$, where $N_{\mathrm{res}} = N_B - 3$, which do not directly couple to the electronic subsystem but are bilinearly coupled to the effective modes. The Hamiltonian of Eqs. (1) and (2) is accordingly modified as follows:

$$\widehat{\boldsymbol{H}}(\widehat{\boldsymbol{q}}_S, \widehat{\boldsymbol{Q}}_B, \widehat{\boldsymbol{Q}}'_B) = \widehat{\boldsymbol{H}}_{\mathrm{eff}}(\widehat{\boldsymbol{q}}_S, \widehat{\boldsymbol{Q}}_B) + \widehat{H}_{B,\mathrm{res}}(\widehat{\boldsymbol{Q}}_B, \widehat{\boldsymbol{Q}}'_B)\mathbf{1}, \tag{6}$$

where the effective-mode portion comprises all vibronic interactions,

$$\widehat{\boldsymbol{H}}_{\mathrm{eff}}(\widehat{\boldsymbol{q}}_S, \widehat{\boldsymbol{Q}}_B) = (\widehat{H}_S^0(\widehat{\boldsymbol{q}}_S) + \widehat{H}_{B,\mathrm{eff}}^0(\widehat{\boldsymbol{Q}}_B))\mathbf{1} + \widehat{\boldsymbol{V}}_{\mathrm{VC}}(\widehat{\boldsymbol{q}}_S, \widehat{\boldsymbol{Q}}_B). \tag{7}$$

The effective and residual parts of the bath Hamiltonian read as follows:

$$\begin{aligned} \widehat{H}_{B,\mathrm{eff}}^0(\widehat{Q}_{B,1}, \widehat{Q}_{B,2}, \widehat{Q}_{B,3}) &= \sum_{i=1}^{3} \frac{\Omega_{B,i}}{2}(\widehat{P}_{B,i}^2 + \widehat{Q}_{B,i}^2) \\ &+ \sum_{i,j=1}^{3} d_{ij}(\widehat{P}_{B,i}\widehat{P}_{B,j} + \widehat{Q}_{B,i}\widehat{Q}_{B,j}) \end{aligned} \tag{8}$$

and

$$\begin{aligned} &\widehat{H}_{B,\mathrm{res}}(\widehat{Q}_{B,1}, \widehat{Q}_{B,2}, \widehat{Q}_{B,3}, \widehat{Q}'_{B,1}, \ldots, \widehat{Q}'_{B,N_{\mathrm{res}}}) \\ &\quad = \sum_{i=1}^{N_{\mathrm{res}}} \frac{\Omega'_{B,i}}{2}(\widehat{P}_{B,i}'^2 + \widehat{Q}_{B,i}'^2) + \sum_{i=1}^{3}\sum_{j=1}^{N_{\mathrm{res}}} d'_{ij}(\widehat{P}_{B,i}\widehat{P}'_{B,j} + \widehat{Q}_{B,i}\widehat{Q}'_{B,j}), \end{aligned} \tag{9}$$

where $\{d_{ij}\}$ defines bilinear couplings within the effective-mode subspace, while $\{d'_{ij}\}$ refers to bilinear couplings between the effective and residual modes.

Alternative choices of effective-mode triples are possible, which result from rotations within the subspace of three effective modes. The choice of topology-adapted modes mentioned above is advantageous when transforming to the adiabatic branching-plane vectors $(\boldsymbol{g}, \boldsymbol{h})$ along with the intersection space vector $\boldsymbol{s}$.[28] In Refs. 26, 27, and 52, preference was given to an alternative construction by which the bilinear couplings between the effective modes are eliminated from Eq. (8).

Likewise, rotations can be carried out in the residual-mode subspace. For example, the frequency matrix $\boldsymbol{\Omega}'$ (with diagonal entries $\Omega'_{B,i}$ and off-diagonal entries d'_{ij}) can be diagonalized in the residual subspace, such that bilinear couplings are exclusively found between effective modes and residual modes. This choice was made in Eq. (9). Alternatively, the bilinear couplings can be cast into a band-diagonal form, leading to a hierarchical electron–phonon model.[29,54] Based on the latter representation, a series of truncation schemes can be introduced, starting with the zeroth-order model where the residual modes are discarded, followed by successive nth order truncations according to the hierarchical chain expansion.

B. Regularized diabatic states (RDS) including collective modes

While the above-mentioned treatment of the environmental modes within the LVC approximation according to Eq. (2) is very useful, there are limitations to this representation. For example, if the system part of the vibronic coupling Hamiltonian Eq. (5) is also reduced to an LVC approximation, the resulting CI seam is necessarily linear, possibly in contrast to the actual situation where a curved CI seam is often encountered. This is why we turn to an improved representation of the combined system–environment vibronic Hamiltonian, specifically using the regularized diabatic states (RDS) construction of Refs. 17 and 18.

The RDS construction removes the singular derivative couplings at a conical intersection and combines an LVC type approximation at the CI with a faithful representation of anharmonic adiabatic potentials at a distance from the CI. In the following, we will focus on symmetry-allowed conical intersections. Adapting the construction of Refs. 17 and 18 to our system, Eq. (5) is replaced with the following diabatic matrix representation with three effective modes:

$$\widehat{\boldsymbol{V}}_{\mathrm{RDS}}(\widehat{\boldsymbol{q}}_S,\widehat{\boldsymbol{Q}}_B)=\widehat{\Sigma}(\widehat{\boldsymbol{q}}_S,\widehat{\boldsymbol{Q}}_B)\mathbf{1}+\frac{\widehat{\Delta}(\widehat{\boldsymbol{q}}_S,\widehat{\boldsymbol{Q}}_B)}{\widehat{\Delta}^{(1)}(\widehat{\boldsymbol{q}}_S,\widehat{\boldsymbol{Q}}_B)}\begin{pmatrix}\widehat{\Delta}_0(\widehat{\boldsymbol{q}}_S,\widehat{\boldsymbol{Q}}_B) & \sum_i\widehat{\lambda}_{S,i}(\widehat{\boldsymbol{Q}}_B)\widehat{q}^{\,c}_{S,i}+\widehat{\Lambda}_B(\widehat{\boldsymbol{q}}_S)\widehat{Q}_{B,3}\\ \sum_i\widehat{\lambda}_{S,i}(\widehat{\boldsymbol{Q}}_B)\widehat{q}^{\,c}_{S,i}+\widehat{\Lambda}_B(\widehat{\boldsymbol{q}}_S)\widehat{Q}_{B,3} & -\widehat{\Delta}_0(\widehat{\boldsymbol{q}}_S,\widehat{\boldsymbol{Q}}_B)\end{pmatrix},\tag{10}$$

where the electronically off-diagonal matrix elements are expanded around a high-symmetry reference geometry and a linearization is carried out for the subsystem coupling modes $\{\widehat{q}^{\,c}_{S,i}\}$. Furthermore, $\widehat{\Sigma}$ and $\widehat{\Delta}$ represent sums and differences of the adiabatic potentials $\widehat{V}_{S_0}$ and $\widehat{V}_{S_1}$

$$\widehat{\Sigma}(\widehat{\boldsymbol{q}}_S,\widehat{\boldsymbol{Q}}_B)\equiv\frac{1}{2}\big(\widehat{V}_{S_0}(\widehat{\boldsymbol{q}}_S,\widehat{\boldsymbol{Q}}_B)+V_{S_1}(\widehat{\boldsymbol{q}}_S,\widehat{\boldsymbol{Q}}_B)\big),\tag{11a}$$

$$\widehat{\Delta}(\widehat{\boldsymbol{q}}_S,\widehat{\boldsymbol{Q}}_B)\equiv\frac{1}{2}\big(\widehat{V}_{S_0}(\widehat{\boldsymbol{q}}_S,\widehat{\boldsymbol{Q}}_B)-\widehat{V}_{S_1}(\widehat{\boldsymbol{q}}_S,\widehat{\boldsymbol{Q}}_B)\big),\tag{11b}$$

and $\widehat{\Delta}^{(1)}$ approximates the difference potential $\widehat{\Delta}$ in the vicinity of the CI,

$$\widehat{\Delta}^{(1)}(\widehat{\boldsymbol{q}}_S,\widehat{\boldsymbol{Q}}_B)=\Bigg(\widehat{\Delta}_0^2(\widehat{\boldsymbol{q}}_S^{\,t},\widehat{\boldsymbol{Q}}_B)+\Bigg[\sum_i\widehat{\lambda}_{S,i}(\widehat{\boldsymbol{Q}}_B)\widehat{q}^{\,c}_{S,i}+\widehat{\Lambda}_B(\widehat{\boldsymbol{q}}_S)\widehat{Q}_{B,3}\Bigg]^2\Bigg)^{1/2},\tag{12}$$

where $\widehat{\Delta}_0(\widehat{\boldsymbol{q}}_S^{\,t},\widehat{\boldsymbol{Q}}_B)$ lies in the high-symmetry subspace,[17,18] in the absence of displacements of the symmetry-breaking modes, i.e., $\{q^c_{S,i}=0\}$ and $Q_{B,3}=0$ [see also Eq. (16) below]. Therefore, an effective LVC model emerges at the CI geometry, which is smoothly connected with a faithful representation of the adiabatic potentials at distant geometries. While the effective environmental modes $\widehat{\boldsymbol{Q}}_B$ are formally derived in the "LVC limit" of the RDS potential [see Eq. (5)], their use in the more general potential of Eqs. (10)–(12) should be understood within a more general diabatization-by-ansatz.

C. Periodic RDS potential and collective energy gap coordinate

For illustration, we now consider a symmetry-allowed conical intersection associated with *cis–trans* isomerization in PSBs in solution, relying on a reduced-dimensional model[47,55] that was adapted to a minimal PSB model system, notably the penta-3,5-dieniminium cation $C_5H_6NH_2^+$.[56,57] Here, a symmetry-breaking torsional coordinate, $\widehat{\phi}$, which acts as a coupling mode, and a symmetry-conserving (tuning) mode $\widehat{r}$ of CC stretch or bond-length alternation type are included, along with a collective energy gap coordinate $\widehat{Q}_{B,2}=\widehat{Q}_{B,-}\equiv\widehat{Q}$.

As further detailed below (Sec. II D), the collective coordinate $\widehat{Q}$ is constructed from a spectral density that conforms to a polar/polarizable solvent, which reacts to the shift of a positive charge in the chromophore following photoexcitation. While the present analysis is restricted to the case of a single collective coordinate rather than the full set of collective modes $\widehat{\boldsymbol{Q}}_B=(\widehat{Q}_{B,1},\widehat{Q}_{B,2},\widehat{Q}_{B,3})$ described in Eq. (10), it is suitable to illustrate the essential concept of integrating collective modes into the RDS construction.

Adiabatic reference potentials, i.e., $V_{S_0}(r,\phi,Q)$ and $V_{S_1}(r,\phi,Q)$, are shown in Fig. 1, constructed as detailed in Sec. S1 in the supplementary material, from a diabatic Hamiltonian set up in a valence bond basis.[47,48] Figure 1(a) shows a curved conical intersection seam, underscoring that an LVC type potential cannot be employed. The snapshots shown in Fig. 1 also illustrate that the solvent configuration determines whether or not a conical intersection is present, such that the solvent dynamics can play a significant role in reaching the intersection. In the NN procedure to be discussed in Sec. III, fitting is carried out for a training dataset sampled from the adiabatic potentials shown in Fig. 1.

The RDS potential is related to the potential that was recently constructed in Ref. 16 in the context of NN fitting. However, in the latter study, we considered a set of intramolecular coordinates rather than a combination of intramolecular and environmental modes, and the RDS construction of Ref. 16 did not account for the periodicity of the PES.

In the present context, the Hamiltonian takes the following form, see Eqs. (6) and (7):

$$\widehat{\boldsymbol{H}}_{\mathrm{RDS}}(\widehat{\phi},\widehat{r},\widehat{Q})=\big(\widehat{H}_S^0(\widehat{\phi},\widehat{r})+\widehat{H}_{\mathrm{eff}}^0(\widehat{Q})+\widehat{H}_{\mathrm{res}}(\widehat{Q}'_1,\ldots,\widehat{Q}'_{N_{\mathrm{res}}})\big)\mathbf{1}+\widehat{\boldsymbol{V}}_{\mathrm{RDS}}(\widehat{\phi},\widehat{r},\widehat{Q}),\tag{13}$$

where $\widehat{\boldsymbol{V}}_{\mathrm{RDS}}$ contains a single effective mode $\widehat{Q}$ as compared with three modes in Eq. (10). Periodicity is introduced in the RDS potential by replacing the linearized form of the ϕ-dependent coupling term by a $\cos\phi$ dependence (similarly to the diabatic reference potential of Ref. 47 as well as related models for retinal isomerization[58]),

$$\widehat{\boldsymbol{V}}_{\mathrm{RDS}}(\widehat{\phi},\widehat{r},\widehat{Q})=\widehat{\Sigma}(\widehat{\phi},\widehat{r},\widehat{Q})\mathbf{1}+\frac{\widehat{\Delta}(\widehat{\phi},\widehat{r},\widehat{Q})}{\widehat{\Delta}^{(1)}(\widehat{\phi},\widehat{r},\widehat{Q})}\times\begin{pmatrix}\widehat{\Delta}_0(\widehat{r},\widehat{Q}) & \widehat{\zeta}(\widehat{r},\widehat{Q})\cos\widehat{\phi}\\ \widehat{\zeta}(\widehat{r},\widehat{Q})\cos\widehat{\phi} & -\widehat{\Delta}_0(\widehat{r},\widehat{Q})\end{pmatrix}.\tag{14}$$

The diabatic coupling $\widehat{\zeta}(\widehat{r},\widehat{Q})$ is expanded around the high-symmetry reference geometry $\cos\phi_0=0$, i.e., $\phi_0=(n-\frac{1}{2})\pi$ for $n=1,2,3,\ldots$, see Eq. (16). The definition of the sum and difference potentials is as before, $\widehat{\Sigma}=\frac{1}{2}(\widehat{V}_{S_0}+\widehat{V}_{S_1})$ and $\widehat{\Delta}=\frac{1}{2}(\widehat{V}_{S_0}-\widehat{V}_{S_1})$; see Eqs. (11a) and (11b). Likewise, $\widehat{\Delta}^{(1)}$ is defined analogously to Eq. (12), with $\cos\phi$ replacing the linearized couplings,

$$\widehat{\Delta}^{(1)}(\widehat{\phi},\widehat{r},\widehat{Q})=\Big(\widehat{\Delta}_0^2(\widehat{r},\widehat{Q})+\widehat{\zeta}^2(\widehat{r},\widehat{Q})\cos^2\widehat{\phi}\Big)^{1/2},\tag{15}$$

where $\widehat{\Delta}_0$ lies in the high-symmetry subspace

$$\widehat{\Delta}_0(\widehat{r},\widehat{Q})=\widehat{\Delta}(\widehat{\phi}=\phi_0,\widehat{r},\widehat{Q})\times\mathrm{sign}\left\{\left.\frac{\partial\widehat{\Delta}(\widehat{\phi},\widehat{r},\widehat{Q})}{\partial\widehat{r}}\right|_{\phi=\phi_0}\right\},\tag{16}$$

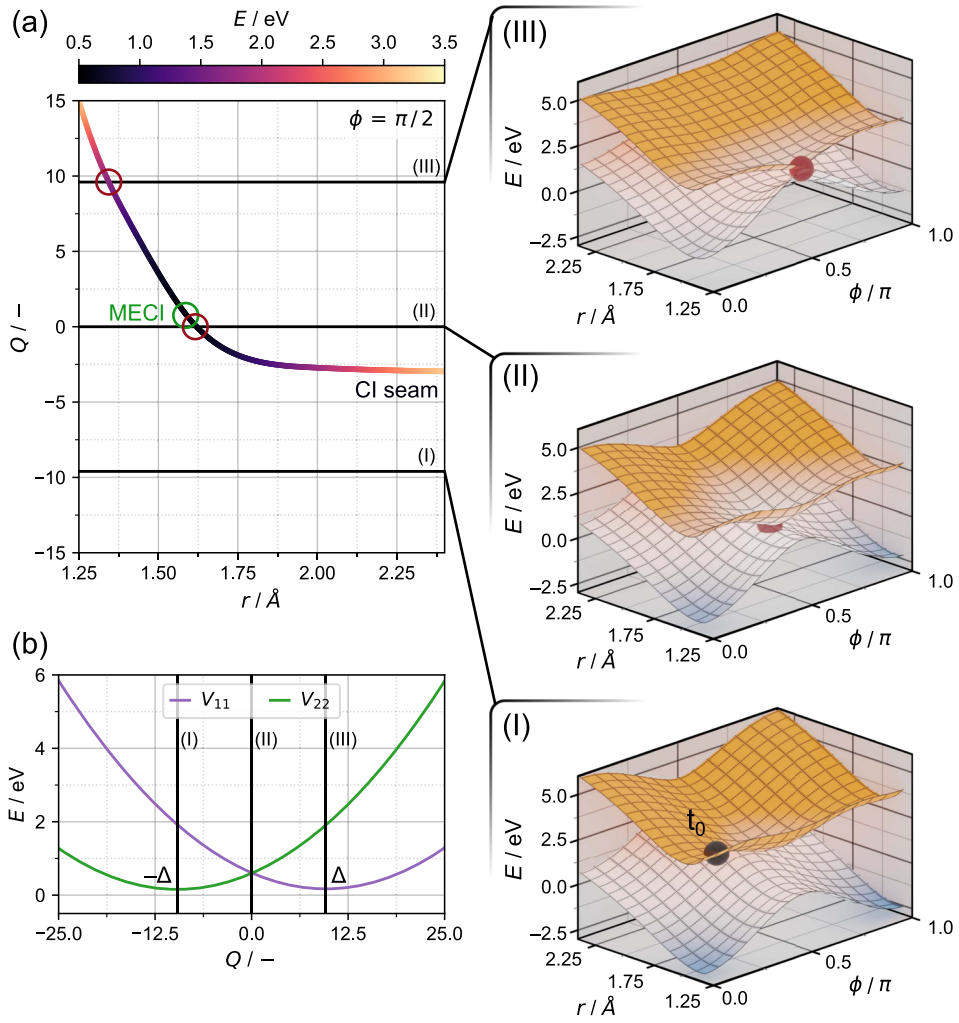

FIG. 1. PES topology for the PSB model system exhibiting a symmetry-allowed conical intersection. The intramolecular coordinates (ϕ, r) and the collective environmental coordinate Q couple to the conical intersection (where Q corresponds to the solvent spectral density J^s to be discussed below). (a) Curved conical intersection seam in the (r, Q) plane. The minimum energy conical intersection (MECI) is marked, and the energy along the seam is color coded. (I)–(III) show the correspondence with a 3D representation of the potential as a function of (r, ϕ); a conical intersection is found in (II) and (III). (b) Diabatic potentials as a function of the Q coordinate.

and $\widehat{\zeta}(\widehat{r},\widehat{Q})$ contains the second derivative of the difference potential with respect to $\cos\phi$, evaluated in the high-symmetry subspace

$$\widehat{\zeta}(\widehat{r},\widehat{Q}) = \left[\frac{1}{2}\frac{\partial^2}{\partial(\cos\widehat{\phi})^2}\widehat{\Delta}^2(\widehat{\phi},\widehat{r},\widehat{Q})\Big|_{\phi=\phi_0,Q=Q_{\mathrm{reg}}}\right]^{1/2}. \quad (17)$$

Note that a regularization is carried out in order to ensure that the second derivative takes positive values; to this end, Q is replaced with $Q_{\mathrm{reg}} = s\Delta_Q \tanh^{-1}\left(\frac{Q}{s\Delta_Q}\right)$, where s is a unitless parameter that is set to 0.5 (see Sec. S2 in the supplementary material).

D. Collective energy gap coordinate and spectral density

While the collective coordinate $\widehat{Q}$ represents the net effect of the environment on the energy gap at the conical intersection, its fluctuation dynamics is determined by the entire set of environmental modes, including all residual modes. In general, the full set of environmental modes is represented by a spectral density $J(\omega)$, which encodes a (quasi-)continuum of environmental states and characterizes the environment's frequency distribution and its couplings to the subsystem.[59] Approximate spectral densities relating to energy gap fluctuations can be determined experimentally[60] or from correlation functions obtained in molecular dynamics simulations.[24] In a quantum setting, the two-point correlation function of the collective Q mode is related to the spectral density by the following Fourier transform relation:[30,31,61]

$$\langle\widehat{Q}(0)\widehat{Q}(t)\rangle = \frac{1}{\pi D^2}\int_{-\infty}^{\infty} d\omega\, J(\omega) n_B(\omega) e^{-i\omega t}, \quad (18)$$

where D is the effective vibronic coupling [see Eq. (5)], $n_B(\omega) = (e^{\omega/(k_BT)} - 1)^{-1}$ is the Bose–Einstein distribution, and the correlation function relates to the equilibrium state of the environment, $C(t) = \langle\widehat{Q}(0)\widehat{Q}(t)\rangle = \mathrm{Tr}\,[\widehat{Q}(0)\widehat{Q}(t)\rho_B^{\mathrm{eq}}]$. The coupling between the collective $\widehat{Q}$ mode and the residual modes $\widehat{Q}'_n$, $n = 1,\ldots,N_{\mathrm{res}}$ is contained in the Heisenberg evolution of the former.

For dielectric relaxation in solution, a Debye-type SD has typically been employed,[31,62] which yields a low-frequency diffuse

SD peak, typically due to reorientational solvent motion, that can be modeled by an overdamped Brownian oscillator model.[30,31] This SD includes both bulk effects and local effects that dominate in the inertial response. Along these lines, variants of the Debye model have been introduced, notably the so-called quantum-overdamped Brownian-oscillator model of Ref. 63,

$$J(\omega) = 4\lambda \frac{\omega\Lambda^3}{(\omega^2+\Lambda^2)^2}, \tag{19}$$

where $\lambda = \pi^{-1}\int_0^\infty d\omega\, \omega^{-1} J(\omega)$ is the reorganization energy and $\Lambda^{-1} = \tau_r$ is the solvent relaxation time scale.[30,60,63] In our study, the above-mentioned SD is going to be employed due to its more pronounced decay as a function of frequency as compared with the Debye SD.[63] In numerical calculations, a discretized form of the SD is employed,

$$J(\omega) = \frac{\pi}{2}\sum_n c_n^2 \delta(\omega-\omega_n), \tag{20}$$

where $c_n = (2\Delta\omega J(\omega_n)/\pi)^{1/2}$ with $J(\omega)$ on the r.h.s. referring to Eq. (19) and $\Delta\omega$ is the frequency spacing for an equidistant frequency distribution of bath oscillators. Beyond the basic equidistant sampling scheme, various improved schemes can be employed[64,65] (see also the discussion in Paper II).[41]

Since the Hamiltonian of Eq. (1) is recast in terms of the Q mode and the residual environmental modes $(Q'_1,\ldots,Q'_{N_{\rm res}})$, see Eqs. (8) and (9), it is convenient to adapt the SD representation accordingly. To this end, the effective-mode frequency is obtained from the SD,[66–68]

$$\Omega = \frac{2}{\pi D^2}\int_0^\infty d\omega\, J(\omega)\omega \simeq \frac{1}{D^2}\sum_n c_n^2\omega_n, \tag{21}$$

which directly relates to the parameter Λ in Eq. (19), i.e., $\Omega = \pi\Lambda/2$ (see Sec. S3 in the supplementary material). Further, the residual spectral density, $J_1(\omega)$, is computed,[66–68] which represents the SD of the remaining modes $(Q'_1,\ldots,Q'_{N_{\rm res}})$ that are coupled to the collective Q coordinate. The residual SD is represented as a collection of harmonic-oscillator modes resulting from a coordinate transformation where all modes are bilinearly coupled to the collective Q mode with couplings $\{d'_{1n}\}$ [see Eq. (9)][29] such that one obtains

$$J_1(\omega) = \sum_{n=1}^{N_{\rm res}} (d'_{1n})^2 \delta(\omega-\Omega'_n), \tag{22}$$

again in mass and frequency weighted coordinates. Figure 2(a) illustrates the SD of Eq. (19) for a "slow" (J^s) vs "fast" (J^f) solvent model, whose SD maxima are located in the low-frequency vs intermediate-frequency range, respectively. Likewise, in Fig. 2(b), the residual SD for these two cases is shown, along with the effective-mode frequencies indicated by the vertical bars. We note that the corresponding solvent relaxation times $\tau_r = \Lambda^{-1} = \pi/(2\Omega)$ lie in the range 50–100 fs (see Sec. S3 in the supplementary material) and are, hence, shorter than typical values ranging from 100 fs to 1 ps.[69] However, experimental evidence[42] suggests ultrafast components of the solvent response in the case of PSB isomerization. In a more complete SD representation, specific underdamped components of the solvent response can be added explicitly.[62]

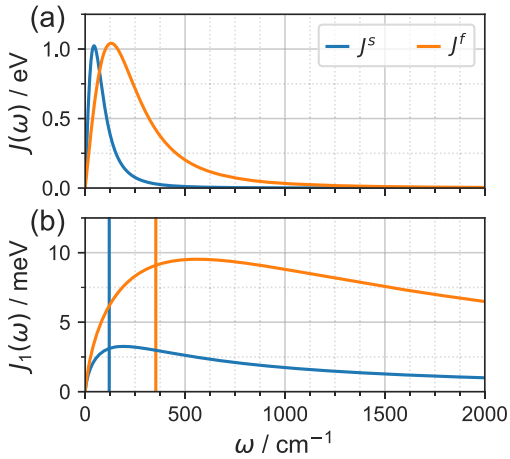

FIG. 2. (a) Representative spectral densities of quantum overdamped Brownian oscillator type, one of which (J^s) (where "s" stands for slow) is centered in the low-frequency range, while the second (J^f) (where "f" stands for fast) is located in the intermediate frequency range. (b) Residual spectral densities according to Eq. (22). The effective-mode frequencies are marked by vertical bars.

III. NEURAL NETWORK APPROACH

Based on the above-mentioned representation of the vibronic potential, NN fitting strategies significantly benefit from the reduced-dimensional nature of the environmental effects on the conical intersection topology. Since the environment-induced vibronic coupling is intrinsically a collective effect, sampling procedures can focus on, e.g., net energy gap fluctuations rather than effects induced by individual environmental modes.

A basic approach, which is adopted in the present work, relates to an NN fit based on a dataset that is strictly limited to the set of vibronically active modes, here (ϕ, r, Q), while the residual modes are taken to be at rest $(Q'_n = 0)$, say, formally at $T = 0$ K. That is, the potential is restricted to the effective-mode part of Eqs. (13) and (14), and it is assumed that data are available as a function of the collective energy gap coordinate Q.

In the present study, the dataset was constructed as follows for the purpose of demonstration of the approach: The original valence-bond reference potential[47] (see Sec. S1 in the supplementary material) was combined with an environmental spectral density of overdamped Brownian oscillator type [see Eq. (19)]. This potential was subsequently recast in RDS form, and the environmental vibronic coupling was subsumed in an effective mode Q according to Eq. (4). Sampling for the NN fit was carried out for the adiabatic potentials obtained by diagonalizing the RDS potential.

In a more flexible setting, sampling would include displacements of all environmental modes, including the residual space, introducing statistical averaging in the collective-mode subspace. The latter perspective, which will be explored in follow-up work, connects to sampling procedures based on atomistic simulations from which energy gap coordinates and their fluctuation dynamics are extracted.[24,70–73] QM/MM calculations in conjunction with trajectory-based dynamics could provide these data.

In the present setting, the NN fit is restricted to the modes (ϕ, r, Q), and coupling to the local baths—acting on both Q and

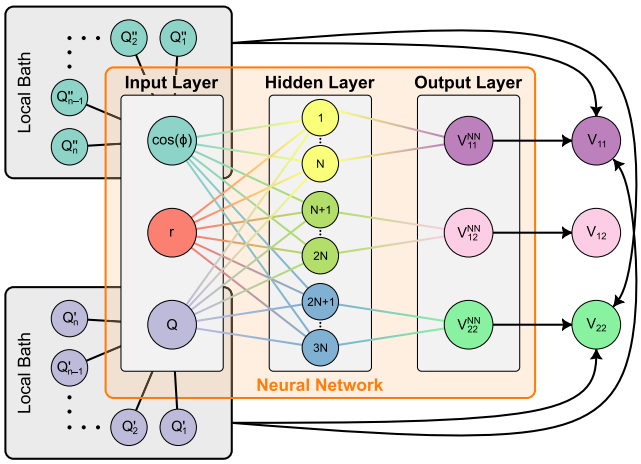

FIG. 3. Schematic illustration of the multiplicative neural network employed in this study. The interactions with the local baths acting on the collective mode Q and the torsional mode ϕ are not part of the NN fit in the present study. The final potential is composed of the NN potential with elements $V_{nm}^{\mathrm{NN}}(\phi, r, Q)$ augmented by these interactions with the local baths.

ϕ—is added at a later stage, as illustrated in Fig. 3. The companion paper illustrates how dynamical calculations are carried out in the combined effective and residual bath spaces at finite temperature, using the TFD approach.

In the following, we outline the main features of the NN procedure, with an emphasis on the aspects that differ from our earlier analysis in Ref. 16.

A. Multiplicative neural networks

While the RDS Hamiltonian Eq. (13) with the potential of Eq. (14) is suitable to carry out quantum dynamical calculations and contains smooth and differentiable potential elements, $\{V_{nm}^{\mathrm{RDS}}\}$, it is not compatible with the sum-of-products (SOP) form of the potential required by tensor network methods like MCTDH. As shown in Ref. 16, a fit to a multiplicative NN potential is a suitable strategy to obtain such SOP potentials, in addition to established potential fit procedures, as employed, e.g., in the context of MCTDH.[35,74]

For a shallow architecture with a simple intermediate (so-called hidden) layer, an approximant for the $\{V_{mn}^{\mathrm{RDS}}\}$ matrix elements in multiplicative NN (m-NN) form is given as follows for a system with f degrees of freedom, $\mathbf{x} = \{x_1, \ldots, x_f\}$:

$$V_{mn}^{\mathrm{RDS}}(\mathbf{x}) \approx V_{mn}^{\mathrm{NN}}(\mathbf{x}) = \mu_{mn}^{(2)} + \sum_{i=1}^{N_{\mathrm{NN}}} \omega_{i,mn}^{(2)} \prod_{d=1}^{f} F_{mn,id}(x_d), \tag{23}$$

where $\mu_{mn}^{(2)}$ and $\omega_{i,mn}^{(2)}$ are the outer-layer weights and biases and F_{mn} is the transfer function, which translates the input variables $\{x_d\}$ via the inner (hidden) layer to the outer layer, i.e., the resulting potential. The transfer function acts as follows:

$$F_{mn,id}(x_d) = F_{mn}\left[\mu_{id,mn}^{(1)} + \omega_{id,mn}^{(1)} x_d\right], \tag{24}$$

where $\omega_{id,mn}^{(1)}$ and $\mu_{id,mn}^{(1)}$ are inner (hidden)-layer weights and biases. Furthermore, N_{NN} denotes the number of NN nodes, which is a crucial parameter for convergence.

Here, we construct a three-dimensional ($f = 3$) PES for the (r, ϕ, Q) subspace, taking into account the periodicity of the PES according to Eq. (14),

$$\begin{aligned} V_{mn}^{\mathrm{RDS}}(\phi, r, Q) &\approx V_{mn}^{\mathrm{NN}}(\phi, r, Q) \\ &= \mu_{mn}^{(2)} + \sum_{i}^{N_{\mathrm{NN}}} \omega_{i,mn}^{(2)} F_{mn,i\phi}(\cos\phi)\, F_{mn,ir}(r) F_{mn,iQ}(Q), \end{aligned} \tag{25}$$

where the individual transfer functions are defined according to Eq. (24). In line with our previous work,[7,16] we choose the following form of the transfer functions:

$$F_{mn}(\tau) = a_{mn} + b_{mn}\tau^2 + c_{mn} e^{-\tau^2}, \tag{26}$$

where the parameters are chosen such as to guarantee that the transfer function is positive definite. A small value of c_{mn} ensures a moderate increase of the function outside of the region covered by sample points, which proved robust in terms of the description of asymptotic properties.[7] For diabatic couplings, V_{mn}, $m \neq n$, Eq. (26) is restricted to a bell-shaped Gaussian function,[16] i.e., $a_{mn} = 0$, $b_{mn} = 0$, $c_{mn} = 1$, as further detailed in Sec. S4 in the supplementary material.

Figure 3 shows a schematic representation of the NN setup, noting that in the present protocol the local baths acting on the coordinates Q and ϕ are not directly included in the NN fit procedure.

B. Multiplicative neural networks: Training protocol

In Ref. 16, we introduced a multi-objective training procedure[75] to account for the fact that the parameter sets $\boldsymbol{\zeta}_{mn} \equiv \left\{\omega_{mn}^{(2)}, \mu_{i,mn}^{(2)}, \omega_{id,mn}^{(1)}, \mu_{id,mn}^{(1)}\right\}$ are interdependent for different (mn) combinations. In this vein, a five-component objective function is used in the present study,

$$Z(\{\boldsymbol{\zeta}_{mn}\}) = \sum_{mn} W_{mn}(\boldsymbol{\zeta}_{mn}) Z_{mn}(\boldsymbol{\zeta}_{mn}) + \sum_{S=S_0,S_1} W_S Z_S(\{\boldsymbol{\zeta}_{mn}\}), \tag{27}$$

where the sum of three individual diabatic sub-objectives $\{Z_{11}, Z_{22}, Z_{12}\}$

$$Z_{mn}(\boldsymbol{\zeta}_{mn}) = \left[\frac{1}{M}\sum_{p}\left(V_{mn}^{\mathrm{NN}}(\phi, r, Q) - V_{mn}^{\mathrm{RDS}}(\phi, r, Q)\right)^2\right]^{1/2}, \tag{28}$$

is complemented by two sub-objectives $\{Z_{S_0}, Z_{S_1}\}$ relating to the adiabatic gradients for $S = S_0, S_1$,

$$Z_S(\{\boldsymbol{\zeta}_{mn}\}) = \left[\frac{1}{M_S}\sum_{p_S}\left|\mathbf{g}_S^{\mathrm{NN}}(\phi, r, Q) - \mathbf{g}_S^{\mathrm{RDS}}(\phi, r, Q)\right|^2\right]^{1/2}, \tag{29}$$

where the adiabatic gradients can be related analytically to the diabatic gradients for the present two-state system (see Sec. S4 in the supplementary material). As in Ref. 16, the diabatic sub-objectives of Eq. (28) were pre-optimized separately, providing initial

conditions for the second step, where the multi-objective optimization according to Eq. (27) is carried out.

The multi-objective function of Eq. (27) differs in several important respects from the objective function employed in Ref. 16. Critically, adiabatic gradient information was restricted to constrained ground-state minima in our previous procedure.[16] As a result, it turned out that constrained S_0 minima suffered from rather large errors that could not be systematically reduced when increasing the number of nodes. This issue is corrected in the present work by including complete gradient information for both states according to Eq. (29). Previous work in the literature has likewise emphasized the importance of including gradient information.[14,76–78]

Furthermore, the CI seam was assigned a separate sub-objective in Ref. 16. While this procedure reproduced the CI seam very well, it turned out in the present analysis that an additional sub-objective was not necessary as long as the gradient information was accurately taken into account. Finally, the weights W [see Eq. (27)] were taken as functions of the full parameter set and were part of the optimization procedure in Ref. 16. In contrast, the weights are reduced to constant parameters in the present procedure, i.e., $W_{nm}(\zeta_{mn}) \equiv W_{nm}$. In fact, we found that the pseudo-weight approach works less efficiently with a larger number of sub-objectives, such that we chose a simpler and more robust version in the present work.

The sampling procedure for the adiabatic potentials $(V_{S_0}(\phi, r, Q), V_{S_1}(\phi, r, Q))$ was similar to Ref. 16, i.e., $M = 10^4$ samples are randomly drawn based on Metropolis sampling from a uniform three-dimensional distribution. Conversion to the diabatic potentials is then carried out according to the RDS construction Eq. (14), with acceptance probabilities $\pi_p = \exp\left(-(V_{mn}(\mathbf{x}_p) - V_{mn}^{\min})/\sigma\right)$, where $\sigma = 0.15$ a.u. Samples for the diabatic coupling $V_{mn}^{\mathrm{NN}}(\mathbf{x}_p)$, $m \neq n$, are taken as a union of the sampling sets for the diagonal elements, resulting in $2M = 2 \times 10^4$ samples.

Symbolic algebra techniques implemented in the SymPy package[79] were employed to analytically derive the RDS potentials and the adiabatic gradients, which were then automatically converted to Fortran90 subroutines for efficient reference data generation. Minimization of the multi-objectives for the NN training utilized the sequential least squares programming (SLSQP) algorithm, as implemented in the SciPy library.[80]

C. Convergence of m-NN fit

With the above-mentioned ingredients, the NN fit quality turns out significantly improved as compared with Ref. 16. Figure 4 shows the RDS diabatic potentials for $N_{\mathrm{NN}} = 30$ nodes, and in Fig. 5, a comparison is shown between the resulting adiabatic neural network PESs as compared with the RDS reference potentials. The adiabatic PESs are accurately reproduced for all regions that are relevant for the dynamics, with average errors around 20 meV. Even the very shallow S_1 minimum at $\phi = n\pi$, $n = 0, \pm 1, \ldots$, and the barrier with a height of ~20 meV are well reproduced. This is not the case, though, for $N_{\mathrm{NN}} < 25$ nodes, where the NN fit produces a saddle point instead of a shallow minimum. Even though this does not significantly affect the dynamics of the present model,[41] the S_1 barrier is an important feature of the PSB potentials, especially in retinal type systems where the barrier height depends on the specific type of retinal PSBs.[45]

Table I illustrates the convergence of the NN-RDS approximants for the stationary points of the adiabatic PESs, as compared with the RDS reference potentials. The global S_0 minimum and the shallow S_1 minimum at $\phi_{\mathrm{eq}} = 0$ (and symmetrically at $\phi_{\mathrm{eq}} = \pi$) are

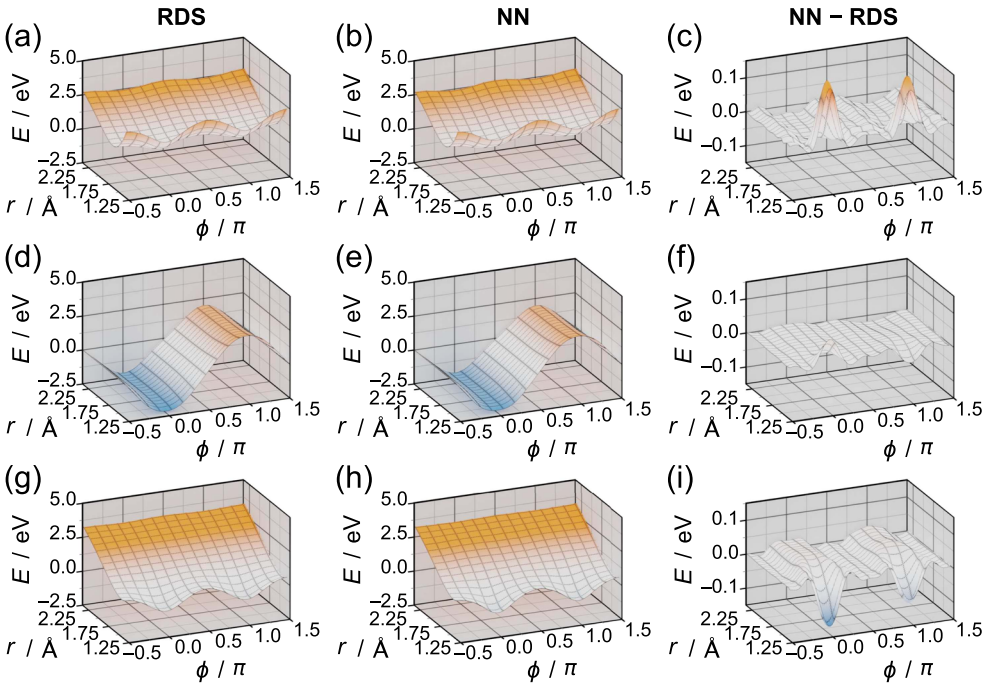

FIG. 4. Comparison between the diabatic RDS potentials and the NN fit ($N_{\mathrm{NN}} = 30$ nodes), along with their difference, shown in the (ϕ, r) subspace at $Q = 0$, for the fast solvent (J^f). (a)–(c) Diagonal potential V_{11}, (d)–(f) coupling function V_{12}, and (g)–(i) diagonal potential V_{22}.

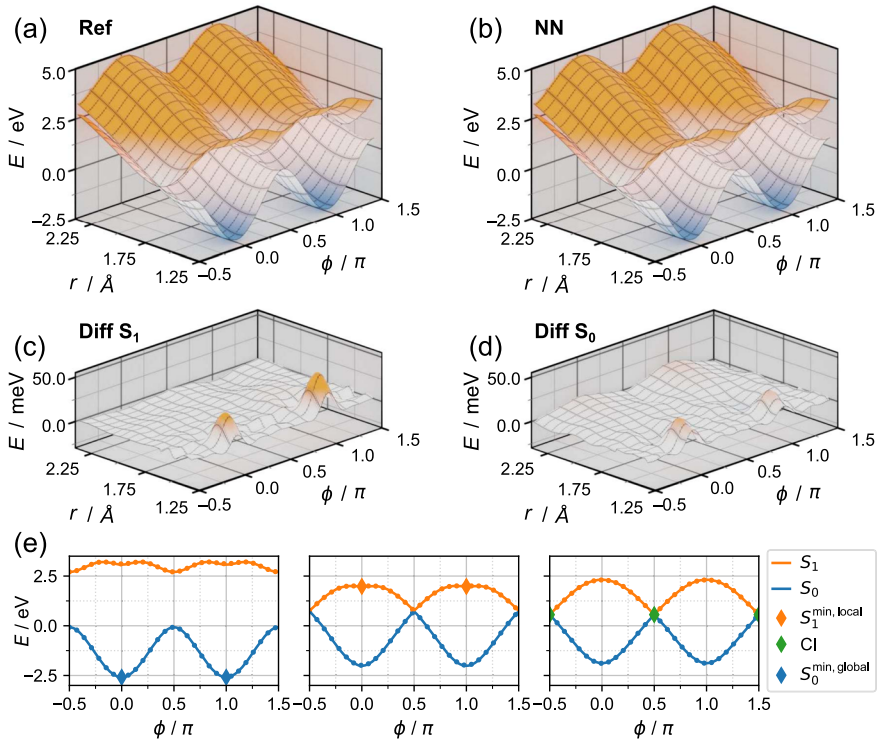

FIG. 5. (a) Adiabatic reference potentials, as compared with (b) NN potentials (N_{NN} = 30 nodes), shown in the (ϕ, r) subspace for Q = 0, for the fast solvent (J^f). The central CI and two neighboring CIs are shown. (c) Difference between the RDS vs NN potentials for the S_1 state, and (d) corresponding difference for the S_0 state. (e) 1D cuts of the adiabatic potentials and their NN approximants [for cuts intersecting the global S_0 minima (left), the local S_1 minima (center), and the CI (right)].

TABLE I. Harmonic vibrational analysis at the stationary points of the adiabatic potentials at ϕ_{eq} = 0 (and symmetrically at $\phi_{eq} = \pi$), for varying numbers of NN nodes and the two SD realizations under study. The global S_0 minimum and the shallow S_1 minimum are considered (see text for details).[a]

			NN						NN				
N_{NN}		S_0 reference	15	20	25	30	35	S_1 reference	15	20	25	30	35
						J^s							
						Stationary point							
ϕ_{eq}	(rad)	0.00	0.00	0.00	0.00	0.00	0.00	0.00	0.00	0.00	0.00	0.00	0.00
r_{eq}	(Å)	1.37	1.34	1.36	1.35	1.36	1.36	1.48	1.50	1.49	1.49	1.49	1.49
Q_{eq}	(−)	−7.62	−7.10	−8.74	−7.96	−7.73	−7.57	4.30	4.03	4.47	4.27	4.23	4.27
						Vibrational frequency							
ω_ϕ	(cm^{-1})	586	548	587	543	573	562	228	177*	175*	109*	92	148
ω_r	(cm^{-1})	1083	969	1072	979	1073	1060	1237	1037	1183	1144	1146	1184
Ω	(cm^{-1})	72	72	75	70	71	72	88	90	89	88	90	90
						J^f							
						Stationary point							
ϕ_{eq}	(rad)	0.00	0.00	0.00	0.00	0.00	0.00	0.00	0.00	0.00	0.00	0.00	0.00
r_{eq}	(Å)	1.37	1.36	1.36	1.36	1.37	1.37	1.48	1.51	1.51	1.50	1.49	1.49
Q_{eq}	(−)	−4.09	−4.55	−4.33	−4.28	−4.15	−3.82	2.41	2.39	2.28	2.47	2.49	2.35
						Vibrational frequency							
ω_ϕ	(cm^{-1})	587	605	596	585	560	562	224	171*	249*	88	129	145
ω_r	(cm^{-1})	1082	1007	1073	1063	1148	1123	1237	1080	1197	1110	1159	1184
Ω	(cm^{-1})	215	217	216	201	221	216	261	261	280	265	264	276

[a]Imaginary frequencies are denoted by an asterisk (*).

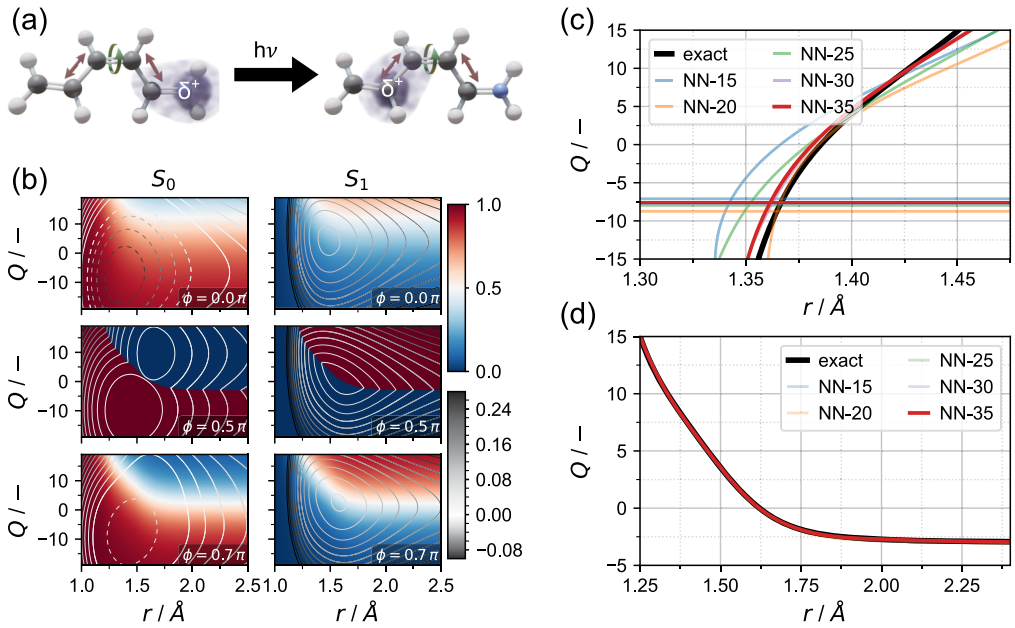

FIG. 6. (a) Illustration of the minimal PSB model under study,[47] exemplified by photoinduced charge translocation in the penta-3,5-dieniminium cation, $C_5H_6NH_2^+$,[56,57] where *cis–trans* isomerization of the central CC bond takes place. The positive charge is localized at the nitrogen end in the S_0 equilibrium geometry and at the carbon end in the S_1 state. (b) Diabatic state character of the RDS potentials as a function of (r, Q), superimposed on the adiabatic S_0 and S_1 PESs. (c) Convergence of the Q-constrained S_0 minima (at $\phi = 0$) as a function of the number of nodes N_{NN}. (d) Convergence of the conical intersection seam as a function of the number of nodes.

considered. The vibrational frequencies at the S_0 minimum are qualitatively reproduced with $N_{NN} = 15$ nodes, and for $N_{NN} = 20$, the S_0 vibrational frequencies are reproduced quantitatively with errors ranging from 1 to 11 cm^{-1}. The equilibrium geometry is almost exactly reproduced for the r and ϕ modes, whereas the Q mode shows up to 15% relative error. For the shallow S_1 minima, convergence is more difficult to achieve, and the frequencies are only qualitatively reproduced at the point where the local topology is captured correctly with $N_{NN} = 25$ (see above).

Figure 6 further shows the convergence of the Q-constrained S_0 minima [panel (c)] and of the CI seam [panel (d)]. The seam is found to converge very well, even for $N_{NN} = 15$, in line with our earlier observations in Ref. 16.

As further detailed in paper II,[41] the scaling of the dynamical calculations using the above-mentioned NN approximants exhibits a near-linear profile as a function of N_{NN}, such that dynamical calculations with highly converged NN-PESs are feasible.

IV. STATISTICAL AVERAGES VIA THERMOFIELDS

We now turn to the inclusion of thermal effects. A typical photochemical scenario involves a thermal reference state pertaining to the solvent equilibrated to the electronic ground state, followed by dynamical evolution that reflects a build-up of chromophore-solvent correlations in the excited state(s). In addition, thermalization should possibly include a subset of intramolecular low-frequency modes. In the context of quantum dynamical simulations at the wave function level, the required thermal ensemble averages can be conveniently represented in terms of an extended, doubled Hilbert space within the Thermofield Dynamics (TFD) approach,[32,33] also denoted purification. This approach leads to an effective thermal Hamiltonian that can be employed in quantum dynamical simulations, as illustrated in Paper II.[41]

In the following, we first summarize the TFD approach (Sec. IV A) and then show how the approach can be tailored to the effective/residual bath representation (Secs. IV B–IV D). In Sec. IV E, we show how the NN potentials of Eq. (25) are combined with the thermalized effective/residual subspaces such as to yield a thermal NN/TFD Hamiltonian, which is going to be used in the quantum dynamical calculations reported in Paper II.[41]

A. Thermofield dynamics

Within the TFD approach, a thermal equilibrium state is represented by a pure state $\widehat{\rho}_T = |\psi_T\rangle\langle\psi_T|$ in a duplicated Hilbert space.[32,33,81] For example, for a single harmonic oscillator, a second, "fictitious" oscillator is introduced, denoted by a tilde symbol,

$$|\psi_T\rangle = Z^{-1/2}(T)\sum_j \exp\left(-\frac{E_j}{2k_BT}\right)|\varphi_j,\widetilde{\varphi}_j\rangle, \tag{30}$$

where Z is the partition function and $|\varphi_j,\widetilde{\varphi}_j\rangle \equiv |\varphi_j\rangle \otimes |\widetilde{\varphi}_j\rangle$ represents a direct product of eigenstates $|\varphi_j\rangle$ of the Hamiltonian, $\widehat{H}|\varphi_j\rangle = E_j|\varphi_j\rangle$, and auxiliary ("tilde") states $|\widetilde{\varphi}_j\rangle$ obeying $\widetilde{H}|\widetilde{\varphi}_j\rangle = E_j|\widetilde{\varphi}_j\rangle$. Here, $\widetilde{H}$ (the "tildian") is chosen to correspond to the same physical system as the reference Hamiltonian and is obtained as $\widetilde{H} = \widehat{H}^\dagger$.[32–34] In fact, there is considerable freedom in the choice of $\widetilde{H}$, but the symmetric choice is advantageous in view of the

transformations discussed below. In this representation, the time evolution is defined in terms of the thermal Hamiltonian $\widehat{H}_T = \widehat{H} - \widetilde{H}$, i.e., $i\hbar\partial_t|\psi\rangle = \widehat{H}_T|\psi\rangle$, where $\partial_t = \partial/\partial t$.

The two-mode pure state of Eq. (30) is also denoted the thermal vacuum state and can be generated from the two-mode vacuum state $|\varphi_0, \widetilde{\varphi}_0\rangle$ by a unitary transformation, i.e., a so-called Bogoliubov transformation[32,33]

$$|\psi_T\rangle = \widehat{T}(\theta)|\varphi_0, \widetilde{\varphi}_0\rangle, \tag{31}$$

with the thermalizing operator,[32,33,85]

$$\widehat{T}(\theta) = e^{-i\widehat{G}(\theta)} = e^{i\theta(\widehat{q}\,\widetilde{p} - \widehat{p}\,\widetilde{q})}, \tag{32}$$

where $\widehat{p} = -i\frac{d}{dq}$, and $\widetilde{p} = i\frac{d}{d\widetilde{q}}$, and $\theta = \operatorname{arctanh}(\exp(-\omega/(2k_BT)))$ is a mixing parameter that depends on the ratio between the oscillator frequency and the thermal energy. The explicit form of Eq. (32) demonstrates that the Bogoliubov transformation involves the mixing between the coordinate and momentum variables of the physical and tilde spaces, leading to a so-called two-mode squeezed vacuum state.[33,82]

Based on Eq. (31), a particularly convenient representation of the time propagation can be found by moving the Bogoliubov transformation from the initial condition to the equations of motion, permitting the use of zero-temperature initial conditions,[33,34]

$$i\hbar\frac{\partial}{\partial t}|\psi\rangle = \widehat{H}_T^{\theta}|\psi\rangle \qquad |\psi(t=0)\rangle = |\varphi_0, \widetilde{\varphi}_0\rangle, \tag{33}$$

where the inverse Bogoliubov transformation (iBT) acts as follows on the thermal Hamiltonian[33,34,83]

$$\widehat{H}_T^{\theta} = \widehat{T}^{\dagger}(\theta)\widehat{H}_T\widehat{T}(\theta) = \widehat{T}^{\dagger}(\theta)(\widehat{H} - \widetilde{H})\widehat{T}(\theta). \tag{34}$$

For example, for an N-mode linear vibronic coupling Hamiltonian, the original Hamiltonian $\widehat{H} = \widehat{H}_{\mathrm{el}} + \widehat{\sigma}_z\sum_n \kappa_n\widehat{q}_n + \sum_n \omega_n/2(\widehat{q}_n^2 + \widehat{p}_n^2)$ translates to the following Bogoliubov transformed TFD Hamiltonian:[34]

$$\widehat{H}_T^{\theta} = \widehat{H}_{\mathrm{el}} + \widehat{\sigma}_z\sum_n (\kappa_n \cosh(\theta_n)\widetilde{q}_n + \kappa_n \sinh(\theta_n)\widetilde{q}_n) + \sum_n \frac{\omega_n}{2}(\widehat{q}_n^2 + \widehat{p}_n^2 - \widetilde{q}_n^2 - \widetilde{p}_n^2). \tag{35}$$

In Eq. (35), use was made of the fact that (i) electronic thermalization can be disregarded and (ii) the vibrational tildian is given as $\widetilde{H}_{\mathrm{vib}} = \frac{1}{2}\sum_n(\widetilde{q}_n^2 + \widetilde{p}_n^2)$, which conveniently allows us to exploit the invariance of $((\widehat{q}_n^2 + \widehat{p}_n^2) - (\widetilde{q}_n^2 + \widetilde{p}_n^2))$ under the Bogoliubov transformation.[33,84]

In the context of the present study, two further issues have to be addressed: first, we will refer to *displaced* harmonic oscillator reference states and, second, the Hamiltonian takes the transformed, hierarchical form of Eqs. (8) and (9) if the residual bath is included. These aspects will be detailed in the following.

B. Thermofields for displaced oscillator states: Collective modes

In the context of vibronic dynamics,[34] the TFD formulation is usually applied to uncorrelated initial reference states where $\widehat{\rho}_T \sim \widehat{\rho}_{\mathrm{el}} \otimes \widehat{\rho}_{\mathrm{vib}}^T$, with $\widehat{\rho}_{\mathrm{vib}}^T$ the thermal bath state in the absence of the electronic subsystem. The extension to correlated system–bath states is feasible but challenging in practice[34] due to the construction of the Bogoliubov transformation. Here, we address an important class of initial vibronic correlations where the equilibrium state of the vibrational subsystem depends on the electronic subsystem. Within a shifted harmonic oscillator model, this requires a modified Bogoliubov transformation relying on a displaced reference state.

To illustrate this issue, we consider the tuning type contribution of the effective mode $\widehat{Q}$ to an LVC Hamiltonian according to Eqs. (5)–(7), i.e., $\widehat{H}_{\mathrm{eff}} = \Omega/2(\widehat{Q}^2 + \widehat{P}^2) + C\widehat{Q}\widehat{\sigma}_z$, and re-write this minimal Hamiltonian for clarity in terms of state-specific shifted harmonic potentials,

$$\widehat{H}_{\mathrm{eff}} = \frac{\Omega}{2}((\widehat{Q} + \Delta)^2 - \Delta^2 + \widehat{P}^2)|0\rangle\langle 0| + \frac{\Omega}{2}((\widehat{Q} - \Delta)^2 - \Delta^2 + \widehat{P}^2)|1\rangle\langle 1|, \tag{36}$$

where $\Delta = C/\Omega$. We now consider a thermal reference distribution pertaining to state $|0\rangle$ or else to state $|1\rangle$, with equilibrium geometry $Q = \pm\Delta$, rather than the standard reference geometry $Q = 0$. In Fig. 1(b), the left and right local diabatic minima exemplify such a reference geometry.

The relevant distribution is generated by a *shifted* Bogoliubov transformation[33,85,86]

$$\widehat{T}_{\Delta}(\theta) = e^{-i\widehat{G}_{\Delta}(\theta)} = e^{i\theta((\widehat{Q}-\Delta)\widetilde{P} - \widetilde{P}(\widehat{Q}-\Delta))}, \tag{37}$$

here for a reference distribution centered at $Q = \Delta$ [i.e., pertaining to state $|1\rangle$ in Eq. (36)]. Note that the present discussion is restricted to real-valued coordinate shifts, while the application of the displacement operator is more general and could include momentum displacements.[33,85,86] As detailed in the Appendix, it turns out that the shifted Bogoliubov transformation of Eq. (37) can be related to the standard Bogoliubov transformation of Eq. (31) via displacement operators $\widehat{D}(\Delta_\theta)$,[85,86] which act such as to induce a shift, $\widehat{D}(\Delta_\theta)\widehat{Q}\widehat{D}^{\dagger}(\Delta_\theta) = \widehat{Q} - \Delta_\theta$. Here, Δ_θ is a temperature-dependent shift,

$$\Delta_\theta = \Delta(1 - e^{-\theta}), \tag{38}$$

such that the following relations hold:

$$\widehat{T}_{\Delta}(\theta) = \widehat{T}(\theta)\widehat{D}^{\dagger}(\Delta_\theta)\widetilde{D}^{\dagger}(\Delta_\theta), \tag{39}$$

and

$$\widehat{T}_{\Delta}^{\dagger}(\theta) = \widetilde{D}(\Delta_\theta)\widehat{D}(\Delta_\theta)\widehat{T}^{\dagger}(\theta). \tag{40}$$

When turning to the iBT framework, the thermal Hamiltonian is now defined with respect to the shifted reference state

$$\widehat{H}_T^{\theta} = \widehat{T}_{\Delta}^{\dagger}(\theta)(\widehat{H} - \widetilde{H})\widehat{T}_{\Delta}(\theta), \tag{41}$$

and can be written similarly to Eq. (35), but replacing $Q \to Q_{\Delta_\theta}$, with $Q_{\Delta_\theta} \equiv Q - \Delta_\theta$,

$$\widehat{H}_{T,\mathrm{eff}}^{\theta} = \widehat{H}_{\mathrm{el}} + \widehat{\sigma}_z(C\cosh(\theta)\widehat{Q}_{\Delta_\theta} + C\sinh(\theta)\widetilde{Q}_{\Delta_\theta}) + \frac{\Omega}{2}(\widehat{Q}_{\Delta_\theta}^2 + \widehat{P}^2 - \widetilde{Q}_{\Delta_\theta}^2 - \widetilde{P}^2). \tag{42}$$

This effective Hamiltonian will be used in the simulations of paper II; however, the reference distribution will be seen to relate to $Q = -\Delta$ according to Fig. 1(b). Next, we consider the indirect effect of the shifted effective-mode equilibrium on the residual bath.

C. Thermofields for displaced oscillator states: Residual bath

Since the equilibrium positions of the residual bath modes depend, in turn, on the effective-mode equilibrium position, the former are also affected by the initial vibronic correlations. In accordance with the bilinear effective-residual mode coupling of Eq. (9), the potential minima of the residual modes are located at $\Delta_n = (D_{1n}/\Omega_n)\Delta$, where $\Delta = C/\Omega$ is the effective-mode shift (and signs would change if the reference distribution is centered at $Q = -\Delta$). Accordingly, a shifted Bogoliubov transformation can be defined as earlier, with thermal shifts for the residual modes, $Q'_n \to Q'_{n,\Delta_\theta}$, with $Q'_{n,\Delta_\theta} \equiv Q - \Delta_{n,\theta}$. The final expression for the thermal Hamiltonian in the effective/residual bath representation reads as follows:

$$\widehat{\boldsymbol{H}}^{\theta}_{T} = \widehat{\boldsymbol{H}}^{\theta}_{T,\mathrm{eff}} + \widehat{H}^{\theta}_{T,\mathrm{res}}\mathbf{1}, \tag{43}$$

where $\widehat{\boldsymbol{H}}^{\theta}_{T,\mathrm{eff}}$ is defined in Eq. (42) and the residual bath contribution is given as

$$\begin{aligned}\widehat{H}^{\theta}_{T,\mathrm{res}} = &\sum_{n=1}^{N_{\mathrm{res}}} \frac{\Omega'_n}{2}\left((\widehat{Q}'_{n,\Delta_\theta})^2 + (\widehat{P}'_n)^2 - (\widetilde{Q}'_{n,\Delta_\theta})^2 - (\widetilde{P}'_n)^2\right)\\ &+ \sum_{n=1}^{N_{\mathrm{res}}} d'_n\Big((\widehat{Q}_{\Delta_\theta}\widehat{Q}'_{n,\Delta_\theta} + \widehat{P}\widehat{P}'_n)\cosh(\theta)\cosh(\theta_n)\\ &+ (\widetilde{Q}_{\Delta_\theta}\widetilde{Q}'_{n,\Delta_\theta} + \widetilde{P}\widetilde{P}'_n)\sinh(\theta)\sinh(\theta_n)\\ &+ (\widehat{Q}_{\Delta_\theta}\widetilde{Q}'_{n,\Delta_\theta} + \widehat{P}\widetilde{P}'_n)\cosh(\theta)\sinh(\theta_n)\\ &+ (\widetilde{Q}_{\Delta_\theta}\widehat{Q}'_{n,\Delta_\theta} + \widetilde{P}\widehat{P}'_n)\sinh(\theta)\cosh(\theta_n)\Big).\end{aligned} \tag{44}$$

In this expression, the coupling terms reflect that both the collective mode and the residual bath are thermalized. Related applications of TFD to chain mappings can be found in Ref. 87.

D. TFD spectral densities

Connecting to Sec. II D, the spectral densities of Eqs. (20) and (22) can be generalized to the thermal Hamiltonian. Referring to an N-mode linear vibronic coupling Hamiltonian, see Eq. (35), thermal spectral densities are defined that correspond to the modified vibronic couplings used in the TFD Hamiltonian,[34,88] i.e.,

$$J^{\theta}(\omega) = \frac{\pi}{2}\sum_n (c^T_n)^2\delta(\omega-\omega_n), \tag{45}$$

and

$$\widetilde{J}^{\theta}(\omega) = \frac{\pi}{2}\sum_n (\widetilde{c}^T_n)^2\delta(\omega-\omega_n), \tag{46}$$

with the thermal vibronic couplings $c^T_n = c_n\cosh\theta$ and $\widetilde{c}^T_n = c_n\sinh\theta$. Likewise, the residual spectral densities of Eq. (22) can be generalized.

The combination of the real and tilde SDs of Eqs. (45) and (46) also constitutes the temperature-dependent quantum noise spectral density,[89–91] where the tilde part is associated with negative frequencies.

In Figs. 7(a) and 7(b), the thermal spectral densities $J^{\theta}(\omega)$ and $\widetilde{J}^{\theta}(\omega)$ are shown for the two representative cases that were presented in Fig. 2. These two cases will be compared in the dynamical simulations discussed in Paper II.[41]

As can be seen from Figs. 7(c)–7(f), the thermalized SDs of Eqs. (45) and (46) take large values in the low-frequency domain where $\omega \sim kT$. Differently from the reference spectral densities (highlighted in blue), the thermal SDs do not decay for $\omega \to 0$, but the real and tilde SDs reach the same, constant values (see Sec. S3 in the supplementary material for details). At $T = 0$ K, the tilde SD vanishes, $\widetilde{J}^{\theta}(\omega) \to 0$, whereas the real SD tends toward the temperature-independent reference SD, $J^{\theta}(\omega) \to J(\omega)$.

E. NN potentials and TFD Hamiltonian

The thermofield approach in the above-mentioned form is tailored to the collective-mode representation of the vibronic

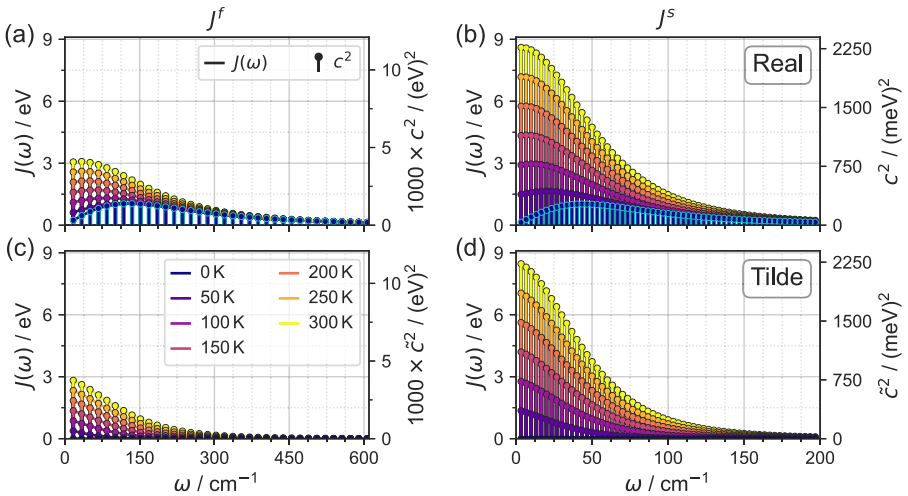

FIG. 7. Thermal spectral densities for the real vs tilde spaces according to Eqs. (45) and (46), for the two relevant SDs shown in Fig. 2(a). Upper panels: Real SD $J^{\theta}(\omega)$ for (a) the fast solvent and (b) the slow solvent; lower panels: tilde SD $\widetilde{J}^{\theta}(\omega)$ for (c) the fast solvent and (d) the slow solvent. The discretized SDs are shown for various temperatures between $T = 0$ K and $T = 300$ K. The reference SDs ($T = 0$ K) are highlighted in blue in (a) and (b).

coupling Hamiltonian discussed in Sec. II D. As demonstrated earlier, the residual environment is consistently included within the assumptions of the underlying spectral density. The resulting thermal Hamiltonian $\widehat{H}_T^\theta$ of Eqs. (42)–(44) is exact if the coupling of the collective mode to the electronic subsystem is described by the LVC form of the interaction. At the same time, $\widehat{H}_T^\theta$ is also expected to represent a good approximation for the thermofields of the collective-mode part within the NN description, recalling that the RDS/NN potentials yield the LVC form of the potential close to the conical intersection. Conversely, obtaining an exact thermal Hamiltonian for the collective mode part of the NN/RDS potentials is possible but rather challenging in practice.[84]

Hence, instead of attempting to obtain an exact thermal Hamiltonian, we opt here for an approximate procedure where the thermofields are approximated in terms of the LVC part of the chromophore–solvent interaction. That is, we augment the NN/RDS potential as follows:

$$\widehat{\boldsymbol{H}}^\theta_{T,\mathrm{NN}}(\widehat{r},\widehat{\phi},\widehat{Q},\widetilde{Q},\{\widehat{Q}'_n\},\{\widetilde{Q}'_n\}) \simeq \widehat{\boldsymbol{H}}_{\mathrm{NN}}(\widehat{r},\widehat{\phi},\widehat{Q}) + \Delta\widehat{\boldsymbol{H}}^\theta_{T,\mathrm{eff}}(\widehat{Q},\widetilde{Q}) + \widehat{H}_{T,\mathrm{res}}(\widehat{Q},\widetilde{Q},\{\widehat{Q}'_n\},\{\widetilde{Q}'_n\})\mathbf{1}, \tag{47}$$

where a thermal correction term is introduced for the collective mode Q and the thermalized residual bath is added. The thermal correction is given as

$$\Delta\widehat{\boldsymbol{H}}^\theta_{T,\mathrm{eff}}(\widehat{Q},\widetilde{Q}) = \widehat{\boldsymbol{H}}^\theta_{T,\mathrm{eff}}(\widehat{Q},\widetilde{Q}) - \widehat{\boldsymbol{H}}_{\mathrm{eff}}(\widehat{Q}), \tag{48}$$

where $\widehat{\boldsymbol{H}}_{\mathrm{eff}}(\widehat{Q})$ represents an LVC approximation to the Q dependence of the NN potential in line with Eq. (36), yielding a "Marcus parabola" type approximation.[24,73] The relevant parameters—i.e., the collective-mode frequency and reorganization energy—can be extracted from the NN fit as detailed in Sec. III. In addition, the shape of the residual SD is taken to be specified, typically according to an overdamped Brownian oscillator model as discussed in Sec. II D.

In fact, the Marcus type approximation is known to be quite robust and typically emerges from anharmonic potentials in atomistic simulations of charge transfer processes.[70–73] Hence, the approximation of Eq. (47) should be valid for typical charge transfer systems. Even so, with a view toward future applications, a natural extension of the NN approach is a generalization to atomistic simulations where the effective/residual-space parameters are obtained for general chromophore–environment interactions.

V. DISCUSSION AND CONCLUSIONS

The present approach is meant for situations where the quantum dynamical evolution of the molecular subsystem—e.g., the chromophore in a photochemical setting—requires a detailed microscopic description and possibly the inclusion of many vibrational modes, while the dynamical effects of the environment can be subsumed in terms of collective coordinates. In the present context, the latter are related to the well-known Brownian oscillator model description and its generalization to effective-mode constructions for conical intersection topologies.[27–29,52] For these situations, the present approach demonstrates how neural network methods in conjunction with flexible quasi-diabatization schemes[17,18] can be applied such as to obtain a consistent chromophore-plus-environment description. Within this description, intramolecular modes and collective environmental modes are treated on equal footing, beyond the linear vibronic coupling model. To this end, we showed how the effective-mode construction of Refs. 27–29 and 52 can be embedded into the quasi-diabatic potentials and, hence, their NN approximants. The collective modes are coupled, in turn, to a residual mode subspace, which contains information on the high-dimensional environment, represented here by an underlying spectral density.

Furthermore, we have shown how the NN potentials can be augmented by thermalization effects in the solvent subspace, such as to obtain a thermal NN Hamiltonian, which is subsequently employed in the quantum dynamical ML-MCTDH calculations of Paper II.[41] At a wave function level, the thermalized state of the environment can be conveniently defined in terms of the thermofield dynamics approach. The latter was adapted to the effective/residual mode partitioning, and it was shown how initial state-specific solvent equilibration (i.e., vibronic correlations) can be described in terms of displaced oscillator states. As discussed in Ref. 84, efficient quantum propagation becomes feasible if low-frequency subsystems are singled out for thermalization. In the present discussion, we focused on the collective-mode subspace in this context, but intramolecular low-frequency modes can obviously be treated similarly.

Against this background, various extensions are feasible. First, the NN construction and quantum dynamical calculations can be straightforwardly generalized to higher-dimensional quantum subsystems. For example, in the context of PSBs, hydrogen out-of-plane modes have been included in reduced-dimensional PESs to obtain a more precise description of the ultrafast isomerization dynamics.[92] To this end, electronic structure data can be sampled either for the isolated or solvated chromophore.

Second, as mentioned earlier, the description of the environment can be made more flexible by introducing atomistic sampling procedures that are not tied to a spectral density model as employed in the present realization. For charge transfer processes in polar/polarizable solvents, it is expected that microscopic energy gap coordinates lead to a similar picture as the one derived here within an SD representation.[24,70–72] In general, though, the dependence on collective environmental coordinates can be more complex, and future developments of the NN/TFD approach will generalize the present framework to account for an atomistic description of the environment. In the case of PSBs, this approach will naturally connect to extensive QM/MM work[20–23] that has been carried out both for solvents and protein environments.

SUPPLEMENTARY MATERIAL

See the supplementary material for information on the reference potentials (Sec. S1), the RDS coupling function (Sec. S2), a detailed analysis of the spectral density (Sec. S3), analytical formulas for the NN gradients (Sec. S4), and further details on the assessment of the accuracy of the NN fit (Sec. S5).

ACKNOWLEDGMENTS

Financial support from the Leverhulme Trust Research Project Grant No. RPG-2023-078 is gratefully acknowledged.

Furthermore, we acknowledge Werner Koch for his contributions to the implementation of the multiplicative neural network approach.

AUTHOR DECLARATIONS

Conflict of Interest

The authors have no conflicts to disclose.

Author Contributions

Bartosz Błasiak: Conceptualization (equal); Data curation (lead); Formal analysis (equal); Investigation (equal); Methodology (equal); Software (lead); Validation (lead); Visualization (supporting); Writing – original draft (supporting); Writing – review & editing (supporting). **Dominik Brey**: Conceptualization (supporting); Data curation (supporting); Formal analysis (supporting); Investigation (supporting); Methodology (supporting); Software (supporting); Validation (supporting); Visualization (lead); Writing – review & editing (supporting). **Rocco Martinazzo**: Conceptualization (supporting); Formal analysis (supporting); Investigation (supporting); Methodology (supporting); Writing – original draft (supporting); Writing – review & editing (supporting). **Irene Burghardt**: Conceptualization (equal); Data curation (supporting); Formal analysis (equal); Funding acquisition (lead); Investigation (equal); Methodology (equal); Project administration (lead); Resources (lead); Supervision (lead); Validation (supporting); Visualization (supporting); Writing – original draft (lead); Writing – review & editing (lead).

DATA AVAILABILITY

The data that support the findings of this study are available from the corresponding author upon reasonable request.

APPENDIX: DERIVATION OF SHIFTED BOGOLIUBOV TRANSFORMATION

In this Appendix, we provide details about the relation Eq. (40) between the shifted Bogoliubov transformation and the standard transformation. We consider the shifted Bogoliubov transformation adapted to a reference coherent state with displacement Δ, see Eq. (37),

$$\widehat{T}_\Delta(\theta) = e^{i\theta((\widehat{Q}-\Delta)\widetilde{P}-\widetilde{P}(\widetilde{Q}-\Delta))}, \tag{A1}$$

where the negative sign of the displacement in the exponential follows from the requirement that the reference coherent state, centered at Δ, is an eigenstate of the shifted annihilation operator, i.e., $((\widehat{Q}-\Delta)+i\sqrt{2}\widehat{P})|\psi_\Delta\rangle = 0$ (see also Ref. 41). Next, we rewrite the exponential as follows:

$$\widehat{T}_\Delta(\theta) \equiv e^{\widehat{A}+\widehat{B}}, \tag{A2}$$

where

$$\begin{aligned}\widehat{A} &= i\theta(\widehat{Q}\widetilde{P}-\widehat{P}\widetilde{Q}),\\ \widehat{B} &= -i\theta\Delta(\widetilde{P}-\widehat{P}),\end{aligned} \tag{A3}$$

noting that the commutator yields

$$[\widehat{A},\widehat{B}] = -i\theta^2\Delta(\widetilde{P}-\widehat{P}) = \theta\widehat{B}. \tag{A4}$$

With Eq. (A4), the transformation of Eq. (A1) can be rewritten using a special case of the Baker–Campbell–Hausdorff formula,[93] i.e.,

$$e^{\widehat{A}+\widehat{B}} = \exp(\widehat{A})\exp\left(\frac{1-e^{-\theta}}{\theta}\widehat{B}\right). \tag{A5}$$

Noting that $\exp(\widehat{A}) = e^{-i\widehat{G}(\theta)} = \widehat{T}(\theta)$, we obtain

$$\begin{aligned}\widehat{T}_\Delta(\theta) &= \widehat{T}(\theta)e^{i(1-e^{-\theta})\Delta(\widehat{P}-\widetilde{P})}\\ &= \widehat{T}(\theta)e^{i\Delta_\theta(\widehat{P}-\widetilde{P})},\end{aligned} \tag{A6}$$

where we defined the thermal coordinate shift Δ_θ, see Eq. (38),

$$\Delta_\theta = \Delta(1-e^{-\theta}). \tag{A7}$$

With the definition of the displacement operators in the real and fictitious spaces,

$$\widehat{D}(\Delta) = \exp(-i\Delta\widehat{P}) \quad ; \quad \widetilde{D}(\Delta) = \exp(i\Delta\widetilde{P}). \tag{A8}$$

Equation (A6) yields

$$\widehat{T}_\Delta(\theta) = \widehat{T}(\theta)\widehat{D}(-\Delta_\theta)\widetilde{D}(-\Delta_\theta), \tag{A9}$$

corresponding to Eq. (40) of the main text.

REFERENCES

[1] W.-K. Chen, X.-Y. Liu, W.-H. Fang, P. O. Dral, and G. Cui, "Deep learning for nonadiabatic excited-state dynamics," J. Phys. Chem. Lett. **9**, 6702–6708 (2018).
[2] J. Westermayr, M. Gastegger, M. F. S. J. Menger, S. Mai, L. González, and P. Marquetand, "Machine learning enables long time scale molecular photodynamics simulations," Chem. Sci. **10**, 8100–8107 (2019).
[3] J. Westermayr and P. Marquetand, "Machine learning and excited-state molecular dynamics," Mach. Learn.: Sci. Technol. **1**, 043001 (2020).
[4] M. S. Chen, T. J. Zuehlsdorff, T. Morawietz, C. M. Isborn, and T. E. Markland, "Exploiting machine learning to efficiently predict multidimensional optical spectra in complex environments," J. Phys. Chem. Lett. **11**, 7559–7568 (2020).
[5] T. Lenzen and U. Manthe, "Neural network based coupled diabatic potential energy surfaces for reactive scattering," J. Chem. Phys. **147**, 084105 (2017).
[6] W. Koch and D. H. Zhang, "Communication: Separable potential energy surfaces from multiplicative artificial neural networks," J. Chem. Phys. **141**, 021101 (2014).
[7] W. Koch, M. Bonfanti, P. Eisenbrandt, A. Nandi, B. Fu, J. Bowman, D. Tannor, and I. Burghardt, "Two-layer Gaussian-based MCTDH study of the $S_1 \leftarrow S_0$ vibronic absorption spectrum of formaldehyde using multiplicative neural network potentials," J. Chem. Phys. **151**, 064121 (2019).
[8] D. M. G. Williams and W. Eisfeld, "Complete nuclear permutation inversion invariant artificial neural network (CNPI-ANN) diabatization for the accurate treatment of vibronic coupling problems," J. Phys. Chem. A **124**, 7608–7621 (2020).
[9] Y. M. Thant, T. Wakamiya, M. Nukunudompanich, K. Kameda, M. Ihara, and S. Manzhos, "Kernel regression methods for prediction of materials properties: Recent developments," Chem. Phys. Rev. **6**, 011306 (2025).
[10] G. W. Richings and S. Habershon, "MCTDH on-the-fly: Efficient grid-based quantum dynamics without pre-computed potential energy surfaces," J. Chem. Phys. **148**, 134116 (2018).
[11] I. Polyak, G. W. Richings, S. Habershon, and P. J. Knowles, "Direct quantum dynamics using variational Gaussian wavepackets and Gaussian process regression," J. Chem. Phys. **150**, 041101 (2019).

[12]H. Köppel, W. Domcke, and L. S. Cederbaum, "Multimode molecular dynamics beyond the Born-Oppenheimer approximation," in *Advances in Chemical Physics* (John Wiley & Sons, Ltd., 1984), pp. 59–246.
[13]D. M. G. Williams and W. Eisfeld, "Neural network diabatization: A new ansatz for accurate high-dimensional coupled potential energy surfaces," J. Chem. Phys. **149**, 204106 (2018).
[14]Y. Guan, H. Guo, and D. R. Yarkony, "Neural network based quasi-diabatic Hamiltonians with symmetry adaptation and a correct description of conical intersections," J. Chem. Phys. **150**, 214101 (2019).
[15]Y. Shu and D. G. Truhlar, "Diabatization by machine intelligence," J. Chem. Theory Comput. **16**, 6456–6464 (2020).
[16]B. Błasiak, D. Brey, W. Koch, R. Martinazzo, and I. Burghardt, "Modelling ultrafast dynamics at a conical intersection with regularized diabatic states: An approach based on multiplicative neural networks," Chem. Phys. **560**, 111542 (2022).
[17]H. Köppel, J. Gronki, and S. Mahapatra, "Construction scheme for regularized diabatic states," J. Chem. Phys. **115**, 2377–2388 (2001).
[18]H. Köppel, "Regularized diabatic states and quantum dynamics on intersecting potential energy surfaces," Faraday Discuss. **127**, 35–47 (2004).
[19]G. J. Atchity, S. S. Xantheas, and K. Ruedenberg, "Potential energy surfaces near intersections," J. Chem. Phys. **95**, 1862–1876 (1991).
[20]M. Ruckenbauer, M. Barbatti, T. Müller, and H. Lischka, "Nonadiabatic photodynamics of a retinal model in polar and nonpolar environment," J. Phys. Chem. A **117**, 2790–2799 (2013).
[21]S. Gozem, H. L. Luk, I. Schapiro, and M. Olivucci, "Theory and simulation of the ultrafast double-bond isomerization of biological chromophores," Chem. Rev. **117**, 13502–13565 (2017).
[22]C. Punwong, J. Owens, and T. J. Martínez, "Direct QM/MM excited-state dynamics of retinal protonated Schiff base in isolation and methanol solution," J. Phys. Chem. B **119**, 704–714 (2015).
[23]E. Pieri, A. R. Walker, M. Zhu, and T. J. Martínez, "Conical intersection accessibility dictates brightness in red fluorescent proteins," J. Am. Chem. Soc. **146**, 17646–17658 (2024).
[24]A. Nitzan, *Chemical Dynamics in Condensed Phases: Relaxation, Transfer, and Reactions in Condensed Molecular Systems* (Oxford University Press, 2014).
[25]V. May and O. Kühn, *Charge and Energy Transfer Dynamics in Molecular Systems*, 3rd ed. (Wiley-VCH, 2011).
[26]L. S. Cederbaum, E. Gindensperger, and I. Burghardt, "Short-time dynamics through conical intersections in macrosystems," Phys. Rev. Lett. **94**, 113003 (2005).
[27]E. Gindensperger, I. Burghardt, and L. S. Cederbaum, "Short-time dynamics through conical intersections in macrosystems. II. Applications," J. Chem. Phys. **124**, 144104 (2006).
[28]I. Burghardt, E. Gindensperger, and L. S. Cederbaum, "An effective Hamiltonian for the short-time dynamics at a conical intersection," Mol. Phys. **104**, 1081–1093 (2006).
[29]I. Burghardt, K. H. Hughes, R. Martinazzo, H. Tamura, E. Gindensperger, H. Köppel, and L. S. Cederbaum, "Conical intersections coupled to an environment," in *Conical Intersections*, edited by W. Domcke, D. R. Yarkony, and H. Köppel (World Scientific, 2011), pp. 301–346.
[30]S. Mukamel, *Principles of Nonlinear Optical Spectroscopy* (Oxford University Press, 1995).
[31]A. Garg, J. N. Onuchic, and V. Ambegaokar, "Effect of friction on electron transfer in biomolecules," J. Chem. Phys. **83**, 4491–4503 (1985).
[32]Y. Takahashi and H. Umezawa, "Thermo field dynamics," Collect. Phenom. **2**, 55 (1975).
[33]S. M. Barnett and P. L. Knight, "Thermofield analysis of squeezing and statistical mixtures in quantum optics," J. Opt. Soc. Am. B **2**, 467 (1985).
[34]R. Borrelli and M. F. Gelin, "Finite temperature quantum dynamics of complex systems: Integrating thermo-field theories and tensor-train methods," Wiley Interdiscip. Rev.: Comput. Mol. Sci. **11**, e1539 (2021).
[35]M. H. Beck, A. Jäckle, G. A. Worth, and H. D. Meyer, "The multiconfiguration time-dependent Hartree (MCTDH) method: A highly efficient algorithm for propagating wavepackets," Phys. Rep. **324**, 1–105 (2000).
[36]H. Wang, "Multilayer multiconfiguration time-dependent Hartree theory," J. Phys. Chem. A **119**, 7951–7965 (2015).
[37]S. R. White and A. E. Feiguin, "Real-time evolution using the density matrix renormalization group," Phys. Rev. Lett. **93**, 076401 (2004).
[38]U. Schollwöck, "The density-matrix renormalization group in the age of matrix product states," Ann. Phys. **326**, 96–192 (2011).
[39]E. W. Fischer and P. Saalfrank, "A thermofield-based multilayer multiconfigurational time-dependent Hartree approach to non-adiabatic quantum dynamics at finite temperature," J. Chem. Phys. **155**, 134109 (2021).
[40]D. Brey, W. Popp, P. Budakoti, G. D'Avino, and I. Burghardt, "Quantum dynamics of electron–hole separation in stacked perylene diimide-based self-assembled nanostructures," J. Phys. Chem. C **125**, 25030–25043 (2021).
[41]B. Błasiak, D. Brey, R. Martinazzo, and I. Burghardt, "Quantum dynamics at a conical intersection in solution. II. Multiconfigurational wavefunction dynamics at finite temperature," J. Chem. Phys. **163**, 124109 (2025).
[42]G. Zgrablić, A. M. Novello, and F. Parmigiani, "Population branching in the conical intersection of the retinal chromophore revealed by multipulse ultrafast optical spectroscopy," J. Am. Chem. Soc. **134**, 955–961 (2012).
[43]G. Bassolino, T. Sovdat, M. Liebel, C. Schnedermann, B. Odell, T. D. W. Claridge, P. Kukura, and S. P. Fletcher, "Synthetic control of retinal photochemistry and photophysics in solution," J. Am. Chem. Soc. **136**, 2650–2658 (2014).
[44]G. Bassolino, T. Sovdat, A. Soares Duarte, J. M. Lim, C. Schnedermann, M. Liebel, B. Odell, T. D. W. Claridge, S. P. Fletcher, and P. Kukura, "Barrierless photoisomerization of 11-cis retinal protonated Schiff base in solution," J. Am. Chem. Soc. **137**, 12434–12437 (2015).
[45]H. V. Kiefer, E. Gruber, J. Langeland, P. A. Kusochek, A. V. Bochenkova, and L. H. Andersen, "Intrinsic photoisomerization dynamics of protonated Schiff-base retinal," Nat. Commun. **10**, 1210 (2019).
[46]J. N. Bull, C. W. West, C. S. Anstöter, G. da Silva, E. J. Bieske, and J. R. R. Verlet, "Ultrafast photoisomerisation of an isolated retinoid," Phys. Chem. Chem. Phys. **21**, 10567–10579 (2019).
[47]I. Burghardt and J. T. Hynes, "Excited-state charge transfer at a conical intersection: Effects of an environment," J. Phys. Chem. A **110**, 11411–11423 (2006).
[48]I. Burghardt, L. S. Cederbaum, and J. T. Hynes, "Environmental effects on a conical intersection: A model study," Faraday Discuss. **127**, 395 (2004).
[49]I. Burghardt, L. S. Cederbaum, and J. T. Hynes, "Ultrafast excited-state charge transfer at a conical intersection: Effects of an environment," Comput. Phys. Commun. **169**, 95–98 (2005), part of Special Issue: proceedings of the Europhysics Conference on Computational Physics 2004: CCP 2004.
[50]J. P. Malhado and J. T. Hynes, "Photoisomerization for a model protonated Schiff base in solution: Sloped/peaked conical intersection perspective," J. Chem. Phys. **137**, 22A543 (2012).
[51]J. P. Malhado, R. Spezia, and J. T. Hynes, "Dynamical friction effects on the photoisomerization of a model protonated Schiff base in solution," J. Phys. Chem. A **115**, 3720–3735 (2011).
[52]E. Gindensperger, I. Burghardt, and L. S. Cederbaum, "Short-time dynamics through conical intersections in macrosystems: I. Theory: Effective mode formulation," J. Chem. Phys. **124**, 144103 (2006).
[53]W. Domcke, D. R. Yarkony, and H. Köppel, *Conical Intersections* (World Scientific, 2004).
[54]H. Tamura, J. G. S. Ramon, E. R. Bittner, and I. Burghardt, "Phonon-driven ultrafast exciton dissociation at donor-acceptor polymer heterojunctions," Phys. Rev. Lett. **100**, 107402 (2008).
[55]I. Burghardt, J. T. Hynes, E. Gindensperger, and L. S. Cederbaum, "Ultrafast excited-state dynamics at a conical intersection: The role of environmental effects," Phys. Scr. **73**, C42–C46 (2006).
[56]M. Garavelli, P. Celani, F. Bernardi, M. A. Robb, and M. Olivucci, "The $C_5H_6NH_2^+$ protonated Schiff base: An *ab initio* minimal model for retinal photoisomerization," J. Am. Chem. Soc. **119**, 6891–6901 (1997).
[57]R. González-Luque, M. Garavelli, F. Bernardi, M. Merchán, M. A. Robb, and M. Olivucci, "Computational evidence in favor of a two-state, two-mode model of the retinal chromophore photoisomerization," Proc. Natl. Acad. Sci. U. S. A. **97**, 9379–9384 (2000).
[58]S. Hahn and G. Stock, "Quantum-mechanical modeling of the femtosecond isomerization in rhodopsin," J. Phys. Chem. B **104**, 1146–1149 (2000).

[59]U. Weiss, *Quantum Dissipative Systems* (World Scientific, 2012).
[60]P. Vöhringer, D. C. Arnett, R. A. Westervelt, M. J. Feldstein, and N. F. Scherer, "Optical dephasing on femtosecond time scales: Direct measurement and calculation from solvent spectral densities," J. Chem. Phys. **102**, 4027–4036 (1995).
[61]I. Burghardt, R. Martinazzo, and K. H. Hughes, "Non-Markovian reduced dynamics based upon a hierarchical effective-mode representation," J. Chem. Phys. **137**, 144107 (2012).
[62]C.-P. Hsu, "Reorganization energies and spectral densities for electron transfer problems in charge transport materials," Phys. Chem. Chem. Phys. **22**, 21630–21641 (2020).
[63]V. Butkus, L. Valkunas, and D. Abramavicius, "Molecular vibrations-induced quantum beats in two-dimensional electronic spectroscopy," J. Chem. Phys. **137**, 044513 (2012).
[64]I. de Vega, U. Schollwöck, and F. A. Wolf, "How to discretize a quantum bath for real-time evolution," Phys. Rev. B **92**, 155126 (2015).
[65]H. Takahashi and R. Borrelli, "Discretization of structured bosonic environments at finite temperature by interpolative decomposition: Theory and application," J. Chem. Theory Comput. **21**, 2206–2218 (2025).
[66]K. H. Hughes, C. D. Christ, and I. Burghardt, "Effective-mode representation of non-Markovian dynamics: A hierarchical approximation of the spectral density. I. Application to single surface dynamics," J. Chem. Phys. **131**, 024109 (2009).
[67]R. Martinazzo, B. Vacchini, K. H. Hughes, and I. Burghardt, "Communication: Universal Markovian reduction of Brownian particle dynamics," J. Chem. Phys. **134**, 011101 (2011).
[68]R. Martinazzo, K. H. Hughes, and I. Burghardt, "Unraveling a Brownian particle's memory with effective mode chains," Phys. Rev. E **84**, 030102(R) (2011).
[69]M. L. Horng, J. A. Gardecki, A. Papazyan, and M. Maroncelli, "Subpicosecond measurements of polar solvation dynamics: Coumarin 153 revisited," J. Phys. Chem. **99**, 17311–17337 (1995).
[70]A. Warshel, "Dynamics of reactions in polar solvents. Semiclassical trajectory studies of electron-transfer and proton-transfer reactions," J. Phys. Chem. **86**, 2218–2224 (1982).
[71]R. A. Kuharski, J. S. Bader, D. Chandler, M. Sprik, M. L. Klein, and R. W. Impey, "Molecular model for aqueous ferrous–ferric electron transfer," J. Chem. Phys. **89**, 3248–3257 (1988).
[72]I. Benjamin, P. F. Barbara, B. J. Gertner, and J. T. Hynes, "Nonequilibrium free energy functions, recombination dynamics, and vibrational relaxation of I_2^- in acetonitrile: Molecular dynamics of charge flow in the electronically adiabatic limit," J. Phys. Chem. **99**, 7557–7567 (1995).
[73]G. K. Schenter, B. C. Garrett, and D. G. Truhlar, "The role of collective solvent coordinates and nonequilibrium solvation in charge-transfer reactions," J. Phys. Chem. B **105**, 9672–9685 (2001).
[74]F. Otto, Y.-C. Chiang, and D. Peláez, "Accuracy of Potfit-based potential representations and its impact on the performance of (ML-)MCTDH," Chem. Phys. **509**, 116–130 (2018).
[75]J. Blank and K. Deb, "Pymoo: Multi-objective optimization in python," IEEE Access **8**, 89497–89509 (2020).
[76]H. T. Nguyen-Truong and H. M. Le, "An implementation of the Levenberg–Marquardt algorithm for simultaneous-energy-gradient fitting using two-layer feed-forward neural networks," Chem. Phys. Lett. **629**, 40–45 (2015).
[77]A. Pukrittayakamee, M. Malshe, M. Hagan, L. M. Raff, R. Narulkar, S. Bukkapatnum, and R. Komanduri, "Simultaneous fitting of a potential-energy surface and its corresponding force fields using feedforward neural networks," J. Chem. Phys. **130**, 134101 (2009).
[78]J. B. Witkoskie and D. J. Doren, "Neural network models of potential energy surfaces: Prototypical examples," J. Chem. Theory Comput. **1**, 14–23 (2005).
[79]P. Virtanen, R. Gommers, T. E. Oliphant, M. Haberland, T. Reddy, D. Cournapeau, E. Burovski, P. Peterson, W. Weckesser, J. Bright, S. J. van der Walt, M. Brett, J. Wilson, K. J. Millman, N. Mayorov, A. R. J. Nelson, E. Jones, R. Kern, E. Larson, C. J. Carey, İ. Polat, Y. Feng, E. W. Moore, J. VanderPlas, D. Laxalde, J. Perktold, R. Cimrman, I. Henriksen, E. A. Quintero, C. R. Harris, A. M. Archibald, A. H. Ribeiro, F. Pedregosa, P. van Mulbregt, A. Vijaykumar, A. P. Bardelli, A. Rothberg, A. Hilboll, A. Kloeckner, A. Scopatz, A. Lee, A. Rokem, C. N. Woods, C. Fulton, C. Masson, C. Häggström, C. Fitzgerald, D. A. Nicholson, D. R. Hagen, D. V. Pasechnik, E. Olivetti, E. Martin, E. Wieser, F. Silva, F. Lenders, F. Wilhelm, G. Young, G. A. Price, G.-L. Ingold, G. E. Allen, G. R. Lee, H. Audren, I. Probst, J. P. Dietrich, J. Silterra, J. T. Webber, J. Slavič, J. Nothman, J. Buchner, J. Kulick, J. L. Schönberger, J. V. de Miranda Cardoso, J. Reimer, J. Harrington, J. L. C. Rodríguez, J. Nunez-Iglesias, J. Kuczynski, K. Tritz, M. Thoma, M. Newville, M. Kümmerer, M. Bolingbroke, M. Tartre, M. Pak, N. J. Smith, N. Nowaczyk, N. Shebanov, O. Pavlyk, P. A. Brodtkorb, P. Lee, R. T. McGibbon, R. Feldbauer, S. Lewis, S. Tygier, S. Sievert, S. Vigna, S. Peterson, S. More, T. Pudlik, T. Oshima, T. J. Pingel, T. P. Robitaille, T. Spura, T. R. Jones, T. Cera, T. Leslie, T. Zito, T. Krauss, U. Upadhyay, Y. O. Halchenko, and Y. Vázquez-Baeza, "SciPy 1.0: Fundamental algorithms for scientific computing in Python," Nat. Methods **17**, 261–272 (2020).
[80]A. Meurer, C. P. Smith, M. Paprocki, O. Čertík, S. B. Kirpichev, M. Rocklin, A. Kumar, S. Ivanov, J. K. Moore, S. Singh, T. Rathnayake, S. Vig, B. E. Granger, R. P. Muller, F. Bonazzi, H. Gupta, S. Vats, F. Johansson, F. Pedregosa, M. J. Curry, A. R. Terrel, Š. Roučka, A. Saboo, I. Fernando, S. Kulal, R. Cimrman, and A. Scopatz, "SymPy: Symbolic computing in Python," PeerJ Comput. Sci. **3**, e103 (2017).
[81]S. M. Barnett and B. J. Dalton, "Liouville space description of thermofields and their generalisations," J. Phys. A: Math. Gen. **20**, 411–418 (1987).
[82]G. J. Milburn, "Multimode minimum uncertainty squeezed states," J. Phys. A: Math. Gen. **17**, 737–745 (1984).
[83]B. Błasiak, D. Brey, R. Martinazzo, and I. Burghardt, "Reduced density matrices and phase-space distributions in thermofield dynamics," arXiv:2505.21302 [quant-ph] (2025).
[84]M. F. Gelin and R. Borrelli, "Thermal Schrödinger equation: Efficient tool for simulation of many-body quantum dynamics at finite temperature," Ann. Phys. **529**, 1700200 (2017).
[85]W.-F. Lu, "Thermalized displaced and squeezed number states in the coordinate representation," J. Phys. A: Math. Gen. **32**, 5037–5051 (1999).
[86]F. A. M. de Oliveira, M. S. Kim, P. L. Knight, and V. Buek, "Properties of displaced number states," Phys. Rev. A **41**, 2645–2652 (1990).
[87]I. de Vega and M.-C. Bañuls, "Thermofield-based chain-mapping approach for open quantum systems," Phys. Rev. A **92**, 052116 (2015).
[88]R. Borrelli and M. F. Gelin, "Simulation of quantum dynamics of excitonic systems at finite temperature: An efficient method based on thermo field dynamics," Sci. Rep. **7**, 9127 (2017).
[89]A. A. Clerk, M. H. Devoret, S. M. Girvin, F. Marquardt, and R. J. Schoelkopf, "Introduction to quantum noise, measurement, and amplification," Rev. Mod. Phys. **82**, 1155–1208 (2010).
[90]D. Tamascelli, A. Smirne, J. Lim, S. Huelga, and M. Plenio, "Efficient simulation of finite-temperature open quantum systems," Phys. Rev. Lett. **123**, 090402 (2019).
[91]H. Takahashi and R. Borrelli, "Effective modeling of open quantum systems by low-rank discretization of structured environments," J. Chem. Phys. **161**, 151101 (2024).
[92]E. Marsili, M. Olivucci, D. Lauvergnat, and F. Agostini, "Quantum and quantum-classical studies of the photoisomerization of a retinal chromophore model," J. Chem. Theory Comput. **16**, 6032–6048 (2020).
[93]B. C. Hall, *Lie Groups, Lie Algebras, and Representations: An Elementary Introduction*, 2nd ed. (Springer International Publishing, 2015), Vol. 222.